2020-02-27

A Novel Association Between Glutamine Metabolism and Clinical Progression in DCMA, A Mitochondrial Cardiomyopathy

King, Melissa Anne

UNIVERSITY OF CALGARY

A Novel Association Between Glutamine Metabolism and Clinical

Progression in DCMA, A Mitochondrial Cardiomyopathy

by

Melissa Anne King

A THESIS

SUBMITTED TO THE FACULTY OF GRADUATE STUDIES

IN PARTIAL FULFILMENT OF THE REQUIREMENTS FOR THE

DEGREE OF MASTER OF SCIENCE

GRADUATE PROGRAM IN BIOLOGICAL SCIENCES

CALGARY, ALBERTA

FEBRUARY, 2020

Abstract

The Dilated Cardiomyopathy with Ataxia Syndrome (DCMA) is a severe mitochondrial disorder with a high rate of mortality. DCMA is caused by mutations in the poorly characterized *DNAJC19* gene which cause a variety of clinical characteristics including elevated 3-methylglutaconic and 3-methylglutaric acids. How these mutations elicit the complex disease presentation is unclear. For this thesis, I developed a fibroblast-based model to study DCMA mitochondrial metabolism. Using stable isotope labeling and metabolomics, I demonstrate that DCMA may be linked to alterations in glutamine catabolism and propose a new model for DCMA involving an inability to import glutamate into the mitochondria. Furthermore, I show that the metabolic phenotype correlates with patient clinical progression. This novel finding could allow clinicians to predict DCMA patient outcomes. This thesis paves the way to reclassifying DCMA as a disorder of glutamine metabolism, and may guide more effective diagnostics for preventing the early death of affected children.

Acknowledgements

Dedication

To my parents Peter and Cora, and to my partner Clark. I could not have done this without you.

Table of Contents

List of Tables

List of Figures and Illustrations

List of Symbols, Abbreviations and Nomenclature

Symbol	Definition
DCMA	Dilated Cardiomyopathy with Ataxia Syndrome
ETC	Electron transport chain
IMM	Inner mitochondrial membrane
ESV	End systolic volume
EDV	End diastolic volume
ATP	Adenosine triphosphate
3-MGA	3-methylglutaconic acid
3-MGA-uria	3-methylglutaconic aciduria
3-MGC	3-methylglutaric acid
TCA	Tricarboxylic acid
α-KG	alpha-ketoglutarate
CO_2	Carbon dioxide
NADH	Nicotinamide adenine dinucleotide
$FADH_2$	Flavin adenine dinucleotide
PMF	Proton motive force
ALT	Alanine aminotransferase
AST	Aspartate aminotransferase
GDH	Glutamate dehydrogenase
MS	Mass spectrometry
LDH	Lactate dehydrogenase
LC-MS	Liquid chromatography-mass spectrometry
NMR	Nuclear magnetic resonance
DMSO	Dimethyl sulfoxide
RPIP	Reverse phase ion pairing
HILIC	Hydrophilic interaction liquid chromatography
TBA	Tributylamine
DMEM	Dulbecco's Modified Eagle Media
FBS	Fetal bovine serum
PBS	Phosphate buffered saline
AGC	Automatic gain control
IT	Injection time
EIC	Extracted ion chromatogram
ppm	Parts per million
HSQC	Heteronuclear single quantum coherence
NH_4Cl	Ammonium chloride
MCL	Multichannel labelling
SEM	Standard error of the mean
MAVEN	Metabolomic analysis and visualization engine
VC	Vehicle control

PPV	Positive predictive value
NPV	Negative predictive value
σ	Standard deviation
X	Average
NCBI	National Center for Biotechnology Information
ROS	Reactive oxygen species
siRNA	Small interfering ribonucleic acid
SS-31	Szeto-Schiller peptide
AMA	Antimycin A

Chapter One: INTRODUCTION

1.1 Overview

The Dilated Cardiomyopathy with Ataxia Syndrome (DCMA) is an inherited genetic disorder

characterized by variable progressive loss of cardiac function, cerebellar ataxia, and growth

failure that results in significant morbidity and mortality in affected children (Davey et al. 2006).

Although the genetic basis of disease is relatively well characterized, the metabolic

underpinnings are not well understood. DCMA is known to be caused by mutations in the

DNAJC19 gene, which encodes a mitochondrial protein of unknown function. DCMA is initially

diagnosed by the presence of elevated 3-methylglutaconic acid and 3-methylglutaric acid

(confirmed by DNA sequencing), and increased production of these compounds is thought to be

connected to abnormal mitochondrial metabolism. In this chapter, I introduce what is currently

known about DNAJC19, its connections to DCMA, and how disruptions in its function could

create the observed clinical phenotypes.

1.2 DCMA

1.2.1 Clinical presentation

      Many heritable metabolic disorders arise from mutations that interfere with mitochondrial

function (Cox 2007). These diseases can feature perturbed central carbon metabolism and are

characterized by systemic problems, frequently in the cardiac and neurological systems

(Schmiedel et al. 2003). For example, Leigh syndrome and other disorders arising from

disabling mutations in the mitochondrial respiratory chain, or electron transport chain (ETC),

prevent normal cellular energy production (Diaz et al. 2011). Human Deafness Dystonia

Syndrome and Spastic Paraplegia-13 are caused by perturbed mitochondrial protein import

preventing the translocation of nuclear-encoded proteins and interfering with mitochondrial

function (MacKenzie and Payne 2007). Another example of such a condition is DCMA, a rare

autosomal recessive inherited disorder that frequently causes early death from heart failure in affected children. With only two reported cases in Finland, one in Turkey and 19 in Canada to date (18 of the cases from Alberta), DCMA is an understudied rare disease (Ojala et al. 2012; Ucar et al. 2016; Al Teneiji et al. 2016; Davey et al. 2006). However, DCMA is relatively common in the Hutterite population of southern Alberta – a genetically isolated and closed religious group (Davey et al. 2006; Sparkes et al. 2007). DCMA causes significant morbidity and mortality in affected children. The clinical hallmarks of DCMA include an enlarged and weakened heart (dilated cardiomyopathy), problems with coordination and balance (ataxia), growth failure, and elevated levels of 3-methylglutaconic acid (3-MGA) and 3-methylglutaric acid (3-MGC) in the urine. Other symptoms which vary from patient to patient include optic atrophy, male genital anomalies, and mild to borderline mental retardation (Davey et al. 2006). Up to 80% of DCMA patients develop dilated cardiomyopathy in the first year of life and, of these patients, 60% ultimately die from heart failure (Al Teneiji et al. 2016). Cardiac dysfunction can range from mild to severe, with severely affected patients potentially requiring mechanical circulatory support and heart transplantation (Rohani et al. 2017). There is currently no diagnostic tool to predict disease progression in this clinically heterogeneous disease. The underlying disease mechanism of DCMA is also currently not understood, which limits the implementation of effective therapy. Previously, medical treatments were based on acquired heart disease seen in adults and were largely ineffective, likely due to the fundamentally different disease mechanisms (Rohani et al. 2017).

In a study conducted at the University of Calgary, Davey et al. identified in 18 patients a homozygous intronic mutation (NM_145261.4(DNAJC19):c.130-1G>C; rs137854888) affecting the splicing of the *DNAJC19* gene, encoding a protein believed to be inserted in the inner mitochondrial membrane (IMM). The mutation results in a shortened, nonfunctional DNAJC19 protein missing helices 1-3 but containing the transmembrane domain (Davey et al. 2006). The

native function of DNAJC19 and therefore the underlying disease mechanism of DCMA is unknown, although it is currently thought to be linked to mitochondrial function due to its proposed insertion into the IMM. Understanding the metabolic underpinnings of DCMA could begin to pave the way to the implementation of effective treatment and the prevention heart failure and death in affected children.

1.2.2 Heart Failure in DCMA

DCMA patient deaths are ultimately caused by intractable heart failure resulting from dilated cardiomyopathy and cardiac dysfunction (Davey et al. 2006). Heart function features powerful twisting movements that allow the ejected blood volume to be efficiently delivered to the body tissues. This is an energy-demanding process and thus limited energy conditions prevent proper contraction of the heart and ultimately lead to the observed DCMA cardiac phenotype (Das 2006; Brown et al. 2017; Squire 1997).

Contraction of the heart (ventricular systole) requires sufficient cellular energy. In energy-limited conditions, there is incomplete ejection of blood from the ventricle. In other words, end-systolic volume (ESV), or the volume of blood present in the ventricles after systole, is increased. During diastole, or relaxation of the ventricles, blood from the body flows back into the ventricles. During diastole, there is maximum distention of the ventricles and the muscle is stretched. An increased ESV will increase the volume of blood left in the ventricles after diastole, or end-diastolic volume (EDV). Increased EDV results in dilated cardiomyopathy due to stretching and weakening of the ventricles (Sequeira and van der Velden 2015; Berk et al. 2005). These impairments in cardiac function due to impaired energy production lead to dilated cardiomyopathy and symptoms and signs of heart failure (Berk et al. 2005; Xie et al. 2012). As cardiac function relies heavily on proper energy production from mitochondrial function,

13

targeting mitochondrial metabolism in DCMA presents an important potential treatment to prevent heart failure in patients (Brown et al. 2017).

1.2.3 DNAJC19

DCMA is caused by nonfunctional DNAJC19, a protein of uncertain function believed to be inserted in the IMM. Based on the BLAST protein sequence database, Davey et al. found that DNAJC19 has homology to the yeast protein Tim14 which suggested that DCMA may be the result of defective mitochondrial protein import (Davey et al. 2006). Tim14 is a component of the Tim23 protein complex, which imports nuclear-encoded proteins into the mitochondrial matrix (Roesch 2002). Furthermore, mammalian DNAJ proteins act as protein chaperones and therefore the DNAJC19 protein may play a role in importing nuclear-encoded proteins into the mitochondria (Sparkes et al. 2007; Stetler et al. 2010). The majority of mitochondrial proteins (99%) are nuclear- encoded and must be imported in an energy-dependent matter (Boengler et al. 2011). Without the ability to properly import proteins, the assembly of necessary complexes (such as the ETC) is inhibited. Since 67 of the 80 ETC subunits are nuclear-encoded, disruptions in mitochondrial protein import will affect ATP production by the ETC and this will prevent efficient mitochondrial respiration (Schmiedel et al. 2003).

A study conducted by Richter-Dennerlein et al. found that DNAJC19 interacts with the mitochondrial prohibitin protein PHB2 and they suggested that this protein-protein interaction regulates cardiolipin metabolism (Richter-Dennerlein et al. 2014). Cardiolipin is a phospholipid unique to the mitochondrial membrane and is synthesized and remodeled within the mitochondrial matrix. Remodeling produces the proper unsaturated acyl tails of the cone-like structure of cardiolipin, which allows for the formation of mitochondrial folds, or cristae, and maximizes mitochondrial respiration capabilities (Ye et al. 2016; Chowdhury et al. 2018). In addition, cardiolipin interacts with the ETC complexes to help them achieve their optimal

structure (Paradies et al. 2014). Mitochondria are responsible for the majority of cellular aerobic energy production in the form of adenosine triphosphate (ATP), the energy currency of the cell (Siasos et al. 2018). Thus, perturbations in cardiolipin remodeling would lead to deficiencies in mitochondrial structure and ATP production (Finsterer 2019). This correlation between mitochondrial structure and function is an important link to consider when investigating the native role of DNAJC19 (Saric et al. 2016).

Richter-Dennerlein et al. found small differences in the relative proportion of cardiolipin species from DNAJC19 knockout cells compared to controls, which may be indicative of perturbed cardiolipin remodeling in DCMA. However, contradictory evidence exists in which levels of cardiolipin species observed in DCMA patient-derived cells were not significantly different from control cells (Rohani et al. 2019; Machiraju et al. 2019). Unaffected cardiolipin suggests normal cardiolipin remodeling in DCMA (Finsterer 2019). Although all of these studies were conducted in different cell types, the *DNAJC19* mutation is ubiquitous and should affect a variety of cell types. Furthermore, the study by Richter-Dennerlein et al. draws its primary conclusions from their finding of a DNAJC19/PHB2 interaction. However, it has been shown that PHB2 weakly and non-specifically interacts with up to 228 proteins (DNAJC19 included) which may explain the observed interaction in their study. Other data has shown that PHB2 only strongly interacts with six other proteins, indicating that PHB2 may not be involved in cardiolipin remodeling with DNAJC19 *in vivo* (Huttlin et al. 2017; Schweppe et al. 2018).

1.2.4 Mitochondria in DCMA

DCMA belongs to a class of diseases defined by elevated levels of 3-MGA and 3-MGC in the plasma and urine and has been classified as type V 3-methylglutaconic aciduria (3-MGA-uria). (Wortmann et al. 2012). Although these phenotypes are diagnostic, the levels of 3-MGA and 3-MGC do not correlate with disease severity (Davey et al. 2006). Increased levels of these

15

organic acids may be indicative of disrupted DNAJC19 function and linked to the underlying

disease mechanism of DCMA. These compounds are thought to be derived from mitochondrial

leucine catabolism but patients with types II-V 3-MGA-uria do not experience elevated urinary 3-

MGA levels after a leucine- or protein-rich meal, suggesting that leucine catabolism may not be

perturbed in these diseases (Wortmann et al. 2012; Jellum et al. 1988). Although type I 3-MGA-

uria is known to be caused by perturbed mitochondrial leucine catabolism, it is currently not

clear how these organic acids are produced in types II-V 3-MGA-uria, and if they are elevated

as a direct result of mitochondrial dysfunction (Wortmann et al. 2012).

An intensively studied and well-characterized disease with a similar clinical phenotype to

DCMA is type II 3-MGA-uria, or Barth Syndrome. Both of these diseases feature abnormal

mitochondrial structure and variable progression of cardiomyopathy (Saric et al. 2016; Machiraju

et al. 2019; Wortmann et al. 2012). Barth syndrome has been shown to be caused by perturbed

cardiolipin remodeling which leads to abnormal mitochondrial structure (Saric et al. 2016). As

discussed previously, perturbations in cardiolipin remodeling would lead to deficiencies in

energy production (Siasos et al. 2018; Finsterer 2019). Although Barth syndrome's clinical

similarities to DCMA seem to suggest that altered mitochondrial structure play a role in DCMA,

normal cardiolipin species present in DCMA-patient derived cells suggest normal cardiolipin

remodeling in DCMA (Machiraju et al. 2019). However, many potential cellular mechanisms can

disrupt mitochondrial structure and function beyond cardiolipin remodeling.

Mitochondria exist in dynamic networks, and mitochondrial energy production is optimal

when these networks are largest, or fused. Breakage or fragmentation of these networks

normally occurs to recycle mitochondria but irregular over-fragmentation can disrupt normal

mitochondrial function (Hoitzing et al. 2015; Scott and Youle 2010). DCMA mitochondria have

been shown to be highly fragmented but this fact alone is not informative regarding the state of

DCMA mitochondrial metabolism and mechanism of disease as the cause of fragmentation is

unknown (Rohani et al. 2017, 2019). Normal cardiolipin in the presence of fragmented

mitochondria in DCMA patient-derived cells suggests that the disease mechanism of DCMA

may lie in mitochondrial structural deficiencies beyond cardiolipin remodeling.

1.3 Mitochondrial metabolism in DCMA

The genetic basis of DCMA has been well characterized and specifically narrowed down to

mutations in the *DNAJC19* gene (Davey et al. 2006). However, the metabolic consequences of

this remain unclear. The presence of 3-MGA and 3-MGC may suggest impaired mitochondrial

metabolism because production of these compounds may be indicative of perturbed

mitochondrial metabolism (Wortmann et al. 2012). The mitochondrial central carbon metabolic

network features glycolysis, the tricarboxylic acid (TCA) cycle, and glutamine catabolism

(Osellame et al. 2012; Gross et al. 2014).

In the cytosol, glucose is catabolized into pyruvate via glycolysis and enters the TCA

cycle as acetyl-CoA (Rogatzki et al. 2015). Historically, it was believed that glucose is a major

contributor to the TCA cycle but recent studies of TCA cycle metabolism have found that

glutamine rather than glucose is a major substrate (Rogatzki et al. 2015; Chen et al. 2018).

Glutamine enters the TCA cycle as alpha-ketoglutarate (α-KG) after a series of metabolic

reactions. The TCA cycle then oxidizes these carbon compounds into carbon dioxide (CO_2) and

passes reducing equivalents in the form of nicotinamide adenine dinucleotide (NADH) or flavin

adenine dinucleotide ($FADH_2$) to the ETC (Fernie et al. 2004). These reducing equivalents

directly link the TCA cycle to ETC function since NADH and $FADH_2$ deposit their electrons at

complex I and II, respectively. High-energy electrons deposited at the ETC are transferred down

the respiratory chain, generating a proton motive force (PMF) across the IMM (Blacker and

Duchen 2016) which ultimately enables mitochondrial ATP synthesis (Mitchell 1961; Maloney et

al. 1974).

Glutamine, on the other hand, is symported with a sodium ion into the cytoplasm then imported directly into the mitochondrial matrix where it undergoes the glutaminase reaction. This reaction deaminates glutamine using a water molecule to produce a free ammonium ion and glutamate. Glutamate can be further deaminated through three different reactions to produce the TCA cycle intermediate α-KG. In the first two reactions, glutamate can be transaminated along with an oxo-acid (pyruvate or oxaloacetate) to produce α-KG and an amino acid (alanine or aspartate). These reactions are, respectively, the alanine and aspartate aminotransferase reactions (ALT and AST). The ALT reaction occurs in the cytosol, and the AST reaction occurs in both the cytosol and mitochondrial matrix, and neither are directly redox-linked (Meléndez-Rodríguez et al. 2019; Conway 2011). The third reaction is the mitochondrial matrix glutamate dehydrogenase (GDH) reaction, which involves an NAD^+ cofactor and is therefore redox-linked. The deamination of glutamate requires NAD^+ and a water molecule to produce NADH, free ammonium, and α-KG (Plaitakis et al. 2017). This reaction can go in either direction, depending on the redox state of the cell (Bhutia and Ganapathy 2016). A diagram demonstrating central carbon metabolism in fibroblasts is shown in Figure 1.1.
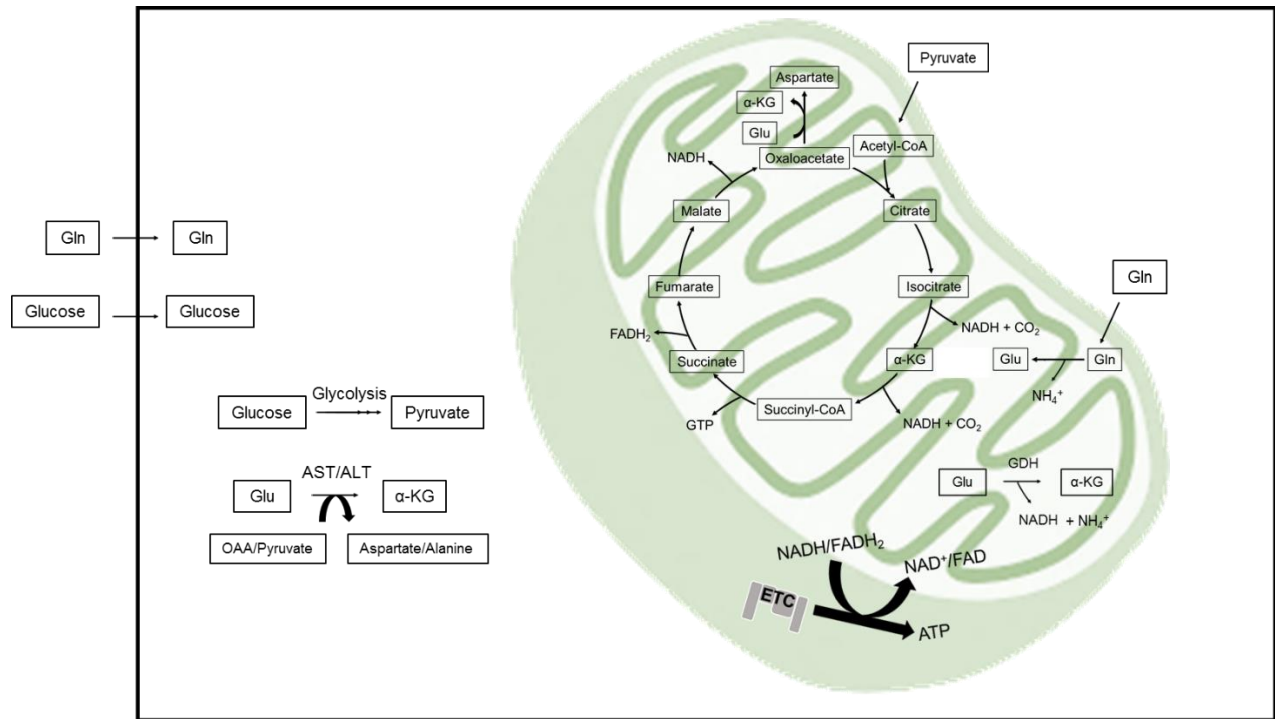
Figure 1.1 Central carbon metabolism in fibroblasts

Glutamine enters the TCA cycle as the intermediate α-KG and glucose-derived acetyl-CoA

enters at the citrate synthase reaction. Oxidative turning of the TCA cycle produces reducing

equivalents that deposit their electrons onto the ETC in the IMM, allowing for ATP synthesis.

The AST, ALT, and GDH reactions are reversible. Information adapted from Conway (2011) and

Plaitakis et al. (2017). Gln represents glutamine; Glu, glutamate; NH4+, ammonium.

To ultimately elucidate the underlying disease mechanism responsible for DCMA, the links between the genetic and metabolic basis of disease must be investigated. Current DCMA models suggest that DNAJC19 is involved in mitochondrial function, perhaps influencing the ability of the ETC to produce ATP. Deficiencies in ETC function have specific consequences on metabolic flux that can be quantified using modern analytical tools.

While concentrations of the metabolites present in cells can be indicative of cellular metabolic state, metabolic flux (reaction turnover rate) is more informative of perturbations in pathways (Jang et al. 2018). Glutamine metabolic flux can be traced *in vitro* by isotope analysis of cultured cells. Stable isotope (^{13}C)-labelled nutrients contain carbon atoms with an extra neutron and these can be differentiated from unlabelled ^{12}C carbons due to the difference in molar mass (Koletzko et al. 1998). Cells growing in isotope-labelled medium become enriched for ^{13}C as the labelled nutrient is metabolized and incorporated into downstream metabolites. This occurs at specific rates, or fluxes, which can be measured over time using mass spectrometry (MS) and kinetic flux profiling (Yuan et al. 2008). Incubating cells with 5-^{13}C labelled glutamine (all five carbons labelled) labels downstream metabolites in a specific way. 5-^{13}C glutamate is produced then 5-^{13}C α-KG, as the carbon backbone remains the same between the three molecules. Oxidative turning of the TCA cycle causes a loss of a ^{13}C atom to the CO_2 produced in the α-KG dehydrogenase reaction, producing 4-^{13}C succinyl-CoA, and then 4-^{13}C succinate after the succinyl-CoA synthetase reaction (Zhang et al. 2014). Reactions downstream of this eventually produce 4-^{13}C oxaloacetate, which is transaminated to aspartate in the AST reaction (Conway 2011). This 4-^{13}C aspartate can be transported out of the mitochondria via the citrin transporter, which also imports glutamate. In the cytosol, aspartate and citrulline form 4-^{13}C argininosuccinate via the argininosuccinate synthetase reaction. Argininosuccinate undergoes the argininosuccinate lyase reaction to produce arginine and 4-^{13}C fumarate, a TCA intermediate (Foschi et al. 2015).

20

In addition to amination, 4-^{13}C oxaloacetate can undergo the citrate synthase reaction. This reaction adds two unlabelled (derived from ^{12}C glucose) carbon acetyl-CoA molecule to oxaloacetate to produce the six-carbon 4-^{13}C labelled citrate molecule which is then isomerized to isocitrate. Isocitrate undergoes the isocitrate dehydrogenase reaction resulting in the loss of a ^{13}C-labelled CO_2 and produces 3-^{13}C α-KG, concluding one oxidative turn of the TCA cycle (Figure 1.2).
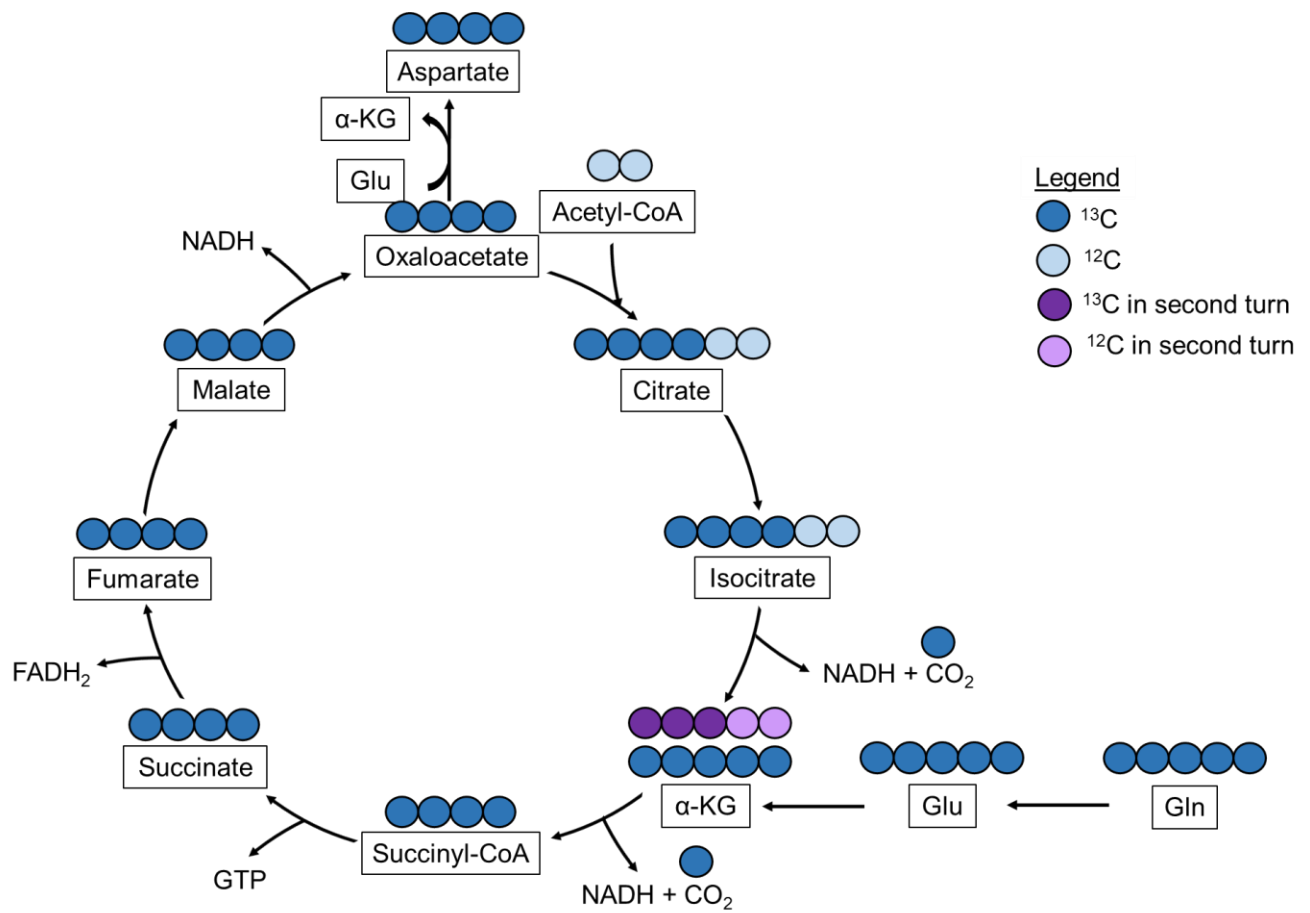
Figure 1.2 Tracing central carbon metabolism with labelled ^{13}C-labelled metabolites.

Darker circles indicate ^{13}C-labelled carbon atoms in various TCA cycle-associated metabolites.

Blue colours indicate labelling of metabolites in the first turn of the TCA cycle, and purple

indicates labelling in the second turn. Glu represents glutamate; GTP, guanine triphosphate.

Current models of DCMA hypothesize that mitochondrial structure is perturbed by the loss of functional DNAJC19 (Richter-Dennerlein et al. 2014; Machiraju et al. 2019). Due to the links between mitochondrial structure and function, there may an inability to produce sufficient cellular energy via mitochondrial function in DCMA (Ikon and Ryan 2017). Deficiencies in mitochondrial function would lead to NADH having to transfer electrons to other acceptors, such as carbon metabolites (Tiefenthaler et al. 2001). One such mechanism is the reverse GDH reaction, which allows for an "electron dump" alternative (rather than electrons being deposited to the ETC) to regenerate NAD^+ for further metabolic reactions and produces glutamate from α-KG. Another reaction is the cytosolic lactate dehydrogenase (LDH) reaction whereby pyruvate is reduced by NADH to regenerate NAD^+ and produce lactate, which is excreted from the cell (Rogatzki et al. 2015). Both of these electron-dumping reactions are sensitive to the redox state of the cell, where in redox stressed conditions, their flux (which regenerates NAD^+) is increased (Siasos et al. 2018). This is because ETC-deficient cells rely more heavily on substrate-level phosphorylation to meet their ATP needs, which requires NAD^+ regeneration (Blacker and Duchen 2016; Chinopoulos and Seyfried 2018).

DCMA is a serious mitochondrial disorder with heterogeneous disease prognosis and whose underlying disease mechanism is unknown. The mutation in *DNAJC19* is expected to perturb normal mitochondrial function and therefore metabolism in DCMA. This is due to not only the proposed subcellular location of DNAJC19 in the IMM but also the proposed native function of DNAJC19 being related to proper mitochondrial structure and function. **Directly investigating the metabolism of DCMA patient-derived cells could provide novel insight into the exact function of DNAJC19 and the underlying disease mechanism.** The current models for DCMA and the role the *DNAJC19* mutation plays in the disease are shown in Table 1.1.

Table 1.1 Current proposed mechanisms explaining the link between the native function of DNAJC19 and the underlying disease mechanism of DCMA.

Proposed DNAJC19 function	Disease mechanism
Nuclear-encoded mitochondrial protein import	Inability to import nuclear-encoded mitochondrial proteins (Davey et al. 2006)
Cardiolipin remodeling	Improper mitochondrial structure due to altered cardiolipin species (Richter-Dennerlein et al. 2014)
Mitochondrial metabolic reactions	Disruptions in mitochondrial metabolism (Wortmann et al. 2012)

1.4 Research hypothesis and aims

A variety of mechanisms have been proposed to explain the connection between the *DNAJC19* mutation and DCMA. However, each of the existing models fail to account for all of the data currently available for DCMA. Applying metabolomics to DCMA introduces an unprecedented perspective into this understudied metabolic disorder. To better understand the unclear metabolic/clinical connection of this disease I developed a novel analytical method for characterizing mitochondrial health through metabolic flux (**Chapter 2**). I then applied this method to conduct a detailed survey of mitochondrial metabolic function in patient-derived fibroblasts across a spectrum of DCMA severities, and introduced a new model for explaining the connection between the *DNAJC19* mutation and DCMA (**Chapter 3**). **From these new data, I propose that the *DNAJC19* mutation perturbs mitochondrial metabolic function through a previously undescribed mechanism: the absence of DNAJC19 disrupts glutamate import into the mitochondrion and thereby disrupts normal carbon and nitrogen fluxes through the organelle.** Characterizing the DCMA metabolic phenotype at the cellular level introduces a novel potential function of DNAJC19.

Chapter Two: DEVELOPING METHODS FOR QUANTIFYING MITOCHONDRIAL HEALTH VIA METABOLIC FLUX IN FIBROBLASTS

2.1 Abstract

There is a wide variety of mitochondrial metabolic disorders with unknown underlying disease mechanisms. To enable clinical characterization of these disorders, I developed a mitochondrial metabolic flux assay that examines mitochondrial health and the effect genetic changes have on mitochondrial function. Conducting kinetic flux profiling yields an assessment of mitochondrial function in an *in vitro* biochemical assay. I developed a hybrid approach utilizing liquid chromatography-mass spectrometry (LC-MS) and nuclear magnetic resonance (NMR) to achieve this purpose. This chapter describes a novel analytical method applied to a fibroblast-based model system which captures all fluxes relevant to glutamine metabolism to study mitochondrial health.

2.2 Introduction

Mitochondrial health can be directly assessed by measuring mitochondrial metabolic flux. Existing tools for measuring metabolism at the cellular level fail to capture crucial elements of mitochondrial boundary fluxes. One example is the Seahorse XF Analyzer®, a technology that measures oxygen consumption and extracellular acidification to infer cellular metabolism (van der Windt et al. 2016; Mookerjee et al. 2015); often coupled with pharmacologic inhibition of the individual ETC subunits. A limitation to this assay is that it indirectly measures metabolism by measuring proton production, which is derived from various metabolic reactions (Zhang et al. 2012). Only through the detection and quantification of metabolites present can one directly measure cellular metabolism. Metabolomics precisely quantifies cellular metabolites and determines pathway flux, and therefore can accurately determine mitochondrial function.

A central metabolic pathway associated with mitochondrial function is the TCA cycle. This pathway is directly linked to mitochondrial energy production (Fernie et al. 2004). Recent research into TCA cycle metabolism has found glutamine to be the primary carbon contributor, as opposed to glucose, in some mammalian cells (Rogatzki et al. 2015; Plaitakis et al. 2017). Glutamine has two critical components: carbon and nitrogen. The metabolic flux of both of these atoms is critical for understanding mitochondrial function. The nitrogen component of glutamine catabolism is ammonium, an ion too small to be detected using LC-MS but detectable by NMR. Unfortunately, NMR does not have the same sensitivity as LC-MS to detect all molecules of interest associated with mitochondrial metabolism. Moreover, NMR is not a tool optimized to calculate flux because it cannot describe isotope enrichment for metabolites. LC-MS is more suited to this purpose as it differentiates molecules based on mass. **However, running LC-MS and NMR studies in parallel presents an effective methodology for studying mitochondrial metabolism.**

Metabolomics using LC-MS and NMR specifically quantifies the metabolites present in a biological sample (Urban 2016). This powerful technology precisely traces how carbon nutrients are metabolized *in vitro* to measure mitochondrial function and health. Glutamine is a primary carbon source that is metabolized in the mitochondrion through central carbon metabolism and thus presents a direct assessment of mitochondrial metabolism (Scalise et al. 2017). Targeted analysis of downstream metabolites produces an assessment of cellular glutamine catabolism. Downstream metabolites are negatively charged (anionic) compounds and are detected and quantified in the extracellular medium. Glutamine metabolism produces TCA cycle intermediates, amino acids such as glutamate and aspartate, and ammonium ions (Scalise et al. 2017). Glutamine-derived isotope enrichment profiles are indicative of carbon usage which is perturbed in cells with deficiencies in mitochondrial energy production (Chen et al. 2018). Quantifying glutamine metabolic flux through quantification of these metabolites

introduces a methodology for an assessment of mitochondrial health. To detect this wide variety of analytes, I adapted and developed three analytical methods in the context of a fibroblast-based model system: 1) LC method adapted from Lu et al. (2010) for detecting anionic TCA cycle intermediates, 2) LC method adapted from Groves (2018) for detecting anionic amino acids and glucose, and 3) NMR method adapted from Ishida (2019) for detecting ammonium ions. Applying these analytical methods to fibroblasts grown in culture quantified cellular glutamine metabolism and assessed mitochondrial health in DCMA cells.

2.3 Methods and Materials

2.3.1 Fibroblast culturing

Fibroblast cultures were isolated from patient skin biopsies provided by the Alberta Precision Laboratories' Genetics & Genomics facility at the Alberta Children's Hospital, ThermoFisher Scientific, and Coriell Institute for Medical Research. Three fibroblast cell lines are from DCMA patients with severe cardiac dysfunction (S1-S3), three from patients with mild cardiac dysfunction (M1-M3), and three unrelated control fibroblast cell lines (C1-C3) (Table 2.1). Two control cell lines C1 and C2 (human dermal fibroblast adult, or hDFa lines) were isolated from healthy adults, and one (C3) was isolated from a healthy control age-matched to severe DCMA patients S1 and S2. Cultures were grown at 37°C in a humidified 5% CO_2 incubator and tissue culture work was conducted in a class II biosafety cabinet. Fibroblasts were grown on tissue culture treated plastic to allow for cell adherence.

Fibroblasts were maintained in T75 treated tissue culture flasks with Dulbecco's Modified Eagle Media (DMEM) containing 25 mM glucose, 2 mM glutamine, phenol red, 100 U/mL penicillin-streptomycin, and 10% fetal bovine serum (FBS) (ThermoFisher Scientific, Sigma-Aldrich). DMEM also contains sodium bicarbonate to maintain a stable pH at 7.4 in a 5% CO_2 incubator (Kostidis et al. 2017). Phosphate buffered saline (PBS) (1x, pH 7.4; ThermoFisher

Scientific) was used to wash cells to remove residual DMEM, and 1.5 mL of 0.5 g/L trypsin-0.2 g/L EDTA solution (Sigma-Aldrich) was used to detach and lift confluent, adherent cells from the flask surface for passaging (split and seeded into a new cell culture vessel). During trypsinization, flasks were incubated for three minutes at 37°C and the side of the flask was gently tapped to assist in cellular detachment. Trypsin neutralizer solution (ThermoFisher Scientific) was used to inhibit the action of trypsin and prevent cellular damage. The cell suspension was centrifuged at 100 x g for 5 minutes, and the cell pellet was resuspended in DMEM. Live cells were counted using a ThermoFisher Scientific Countess II FL automated cell counter and passaged or frozen down (in the latter case, resuspended in freezing medium containing 10-20% dimethyl sulfoxide (DMSO) (Cell Applications, Inc.)). Frozen cells in cryovials were cooled overnight at -80°C in a 2-propanol bath for a slow cooling rate of -1°C/min, and then were transferred to liquid nitrogen storage. Medium was changed every 4-7 days until cells reached ≥80% confluency and were passaged up to 20 passages. Past this passage number, fibroblasts begin to show signs of cellular aging and the metabolic phenotypes they exhibit may not be representative of the original patient-derived phenotype (Boraldi et al. 2010; Janson et al. 2013).

For metabolomics experiments, maintenance DMEM was changed to stable isotope-labelled DMEM. This experimental DMEM contains the same components as the maintenance DMEM, except with 2 mM dual stable isotope-labelled ($5\text{-}^{13}C$ $2\text{-}^{15}N$) glutamine (Cambridge Isotope Laboratories, Inc.), 5.5 mM glucose, no phenol red (which can disrupt metabolism), and 10% dialyzed FBS (ThermoFisher Scientific); dialysis of FBS removes small molecules that may interfere with cellular metabolism and MS analysis, such as amino acids, hormones, and cytokines (Zhang et al. 2014). Experimental glucose concentration was lowered from 25 to 5.5 mM to better represent *in vivo* glucose levels (Lemons et al. 2010). Extracellular and

intracellular glutamine metabolic fluxes were determined using isotope analysis as described in

Chapter 2.3.6 and 2.3.7, respectively.

Table 2.1 Established fibroblast cell lines and their corresponding phenotype based on patient cardiac dysfunction.

Cell line name	Phenotype
S1	Severe DCMA
S2	Severe DCMA
S3	Severe DCMA
M1	Mild DCMA
M2	Mild DCMA
M3	Mild DCMA
C1	Control
C2	Control
C3	Control

Biological samples were kept in the mass spectrometer autosampler at 4°C to minimize degradation of metabolites. 2 µL of samples were injected onto an LC column which gradually (flow rate of 0.6 mL/minute) loads metabolites into a ThermoFisher Scientific Q Exactive Basic Orbitrap Mass Analyzer. Metabolites have diverse chemical properties and thus require different LC methods for their separation for accurate measurement.

An LC gradient of aqueous versus nonpolar solvents separates metabolites within a complex biological mixture for accurate quantification. LC methods were developed and adjusted to allow for detection of the desired metabolites. A reverse phase ion pairing (RPIP) LC method adapted from Lu et al. (2010) detected anionic TCA cycle intermediates, and a hydrophilic interaction liquid chromatography (HILIC) LC method detected anionic polar compounds that are not sufficiently retained using the RPIP LC method, such as amino acids or glucose (Lu et al. 2010). Standards were run in the same matrix as spent medium samples to minimize matrix effects, which can cause variance in signal intensities given the same concentration of a metabolite (Silvestro et al. 2013). Running external standard curves of target compounds verifies the identity of MS signals.

2.3.2 Detection of TCA cycle intermediates using a modified RPIP method

An existing RPIP LC method using tributylamine (TBA) as an ion pairing reagent was modified to quantify and detect anionic TCA cycle metabolites (Lu et al. 2010). The mobile phase of TBA-containing solvent was run through the stationary phase, an Agilent Zorbax RRHD SB-C18 1.5 µM threaded column. For this study, all metabolite standards (Sigma-Aldrich) were prepared in DMEM with no glucose or glutamine containing 10% dialyzed FBS and diluted 20-fold into 50% methanol to match the matrix of biological samples for accurate quantification.

32

The LC method developed uses a four stage linear gradient with 97:3 water:methanol with 10 mM TBA and 15 mM acetic acid adjusted to pH 7.5 as solvent A, and 100% acetonitrile as solvent D (Lu et al. 2010) (Figure 2.1). Glacial acetic acid or sodium hydroxide were used for all solvent pH adjustments. The gradient starts with 100% polar solvent A and gradually ramps to 100% nonpolar solvent D, allowing anionic TCA cycle metabolites to interact with and bind to the positively charged TBA on the column, then elute with the TBA with acetonitrile. Acetonitrile removes the charge from the TBA by increasing the pH of the solvent, releasing metabolites from the ion-pairing reagent. The modified RPIP method was run in negative mode and the mass spectrometer parameters are as follows: resolution of 140,000, automatic gain control (AGC) target of 1e6, maximum injection time (IT) of 200 ms, and scan range of 70-1000 m/z.
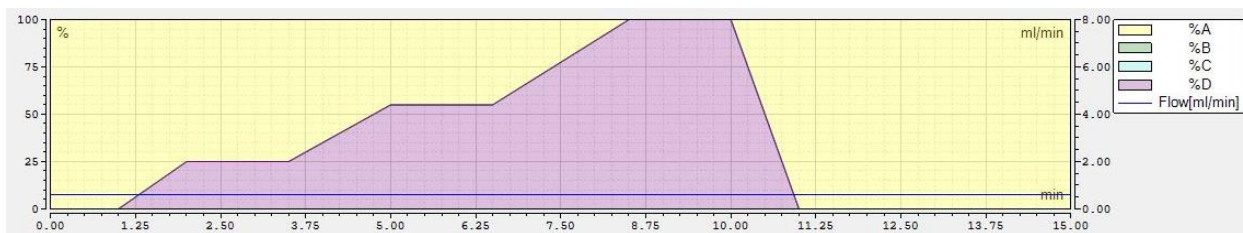
Figure 2.1 RPIP LC gradient

The x-axis represents time in minutes and the y-axis represents percentage of solvents A (yellow) or D (pink) running through a C18 column. The gradient is 0 min, 0% D; 1 min, 0% D; 2 min, 25 % D; 3.5 min, 25% D; 5 min, 55% D; 6.5 min, 55% D; 8.5 min, 100% D; 10 min, 100% D; 11 min, 0% D. The flow rate is 600 μL/min and total run time is 15 minutes. Solvent A is 97:3 methanol:water with 10 mM TBA and solvent D is 100% acetonitrile. This figure was obtained using ThermoFisher Scientific Xcalibur software.

2.3.3 Detection of amino acids and glucose using an adapted HILIC method

A method for detecting and quantifying amino acids was adapted from Groves and optimized by testing solvents and pH values that yielded the highest peak intensity and an accurate linear range for compounds. A ThermoFisher Scientific Syncronis HILIC HPLC column was used as the stationary phase, while the mobile phase of 20 mM ammonium formate at pH 3.0 as the aqueous or polar solvent (solvent C), and acidified acetonitrile (with0.1% formic acid) as the nonpolar solvent (solvent B). The HILIC method uses a three-stage gradient (Figure 2.2). Unlike the RPIP method, the HILIC method starts with nonpolar solvent B where polar metabolites are retained on the polar HILIC column and do not interact with the nonpolar solvent. Gradually increasing polar solvent C elutes the polar metabolites from the column. The adapted HILIC method was run in negative mode and the mass spectrometer parameters are as follows: resolution of 140,000, AGC target of 3e6, maximum IT of 200 ms, and scan range of 70-1000 m/z.
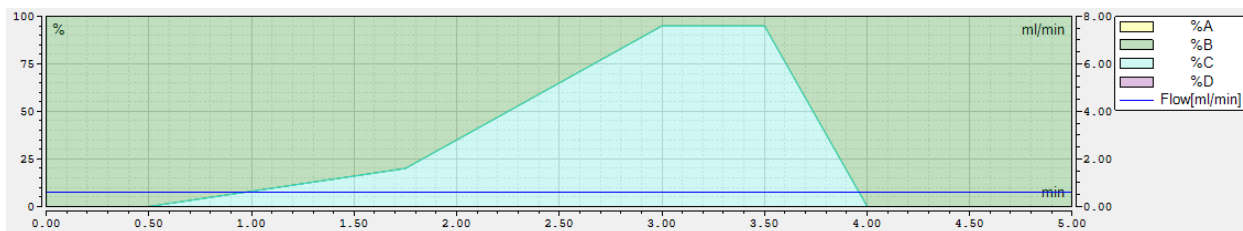
Figure 2.2 HILIC LC gradient.

The x-axis represents time in minutes and the y-axis represents percentage of solvents B (green) or C (blue) running through a HILIC column. The gradient is 0 min, 0% C; 0.5 min, 0% C; 1.75 min, 20 % C; 3 min, 95% C; 3.5 min, 95% C; 4 min, 0% C; 5 min, 0% C. The flow rate is 600 μL/min and total run time is 5 minutes. Solvent B is 100 % acetonitrile with 0.1% formic acid and solvent C is 20 mM ammonium formate pH 3.0. This figure was obtained using ThermoFisher Scientific Xcalibur software.

2.3.4 LC-MS data processing

ThermoFisher Scientific Xcalibur .RAW files were converted to .MZXML files and analyzed using MAVEN software as extracted ion chromatograms (EICs). Peaks were picked with the following MAVEN settings: parts per million (ppm) window (5.00), signal intensity value (AreaTop), EIC smoothing algorithm (Savitzky-Golay), EIC smoothing window (10 scans), max retention time difference between peaks (0.50 min), and ionization (-1). The identity of peaks was confirmed with a known peak library list loaded into MAVEN to match compounds with their mass to charge ratios, and peak identities were further confirmed by external standards. Data were exported as Microsoft Excel .CSV files with raw signal intensities and used to generate standard curves. Statistics were done using Student's two-tailed t-test (with Gaussian Approximation if populations failed a D'Agostino and Pearson omnibus normality test).

2.3.5 Detection of ammonium using 1D HSQC NMR

Ammonium ions are too small in molar mass to be detected by MS, and NMR yields reproducible results across samples (Kostidis et al. 2017). Extracellular ^{15}N-labelled ammonium was detected and quantified using proton 1D ^{1}H ^{15}N heteronuclear single quantum coherence (HSQC) NMR spectroscopy in a method adapted by Ishida. Spent medium (after 24 h incubation) in 10% D_2O was adjusted to pH 3 in sample preparation; the pH value found to give the highest signal for ammonium detection between pH 2-7. A 600 MHz Bruker NMR spectrometer was used to conduct 1D ^{1}H ^{15}N HSQC NMR spectroscopy. Samples were run at 298 K, and each sample was shimmed and the 90° pulse adjusted. ^{15}N ammonium chloride (NH_4Cl) and glutamine standards confirmed the NMR spectra peaks at 7.01 ppm for ^{15}N ammonium, and 7.52 and 6.81 ppm for ^{15}N glutamine (Figure 2.3). For this study, metabolite standards (Cambridge Isotope Laboratories, Inc.) were prepared in DMEM containing 10% dialyzed FBS in 10% D_2O to match the matrix of biological samples for accurate quantification.

All NMR spectra were processed using TopSpin version 4.0.7 and absolute integral values were exported as Microsoft Excel .csv files.
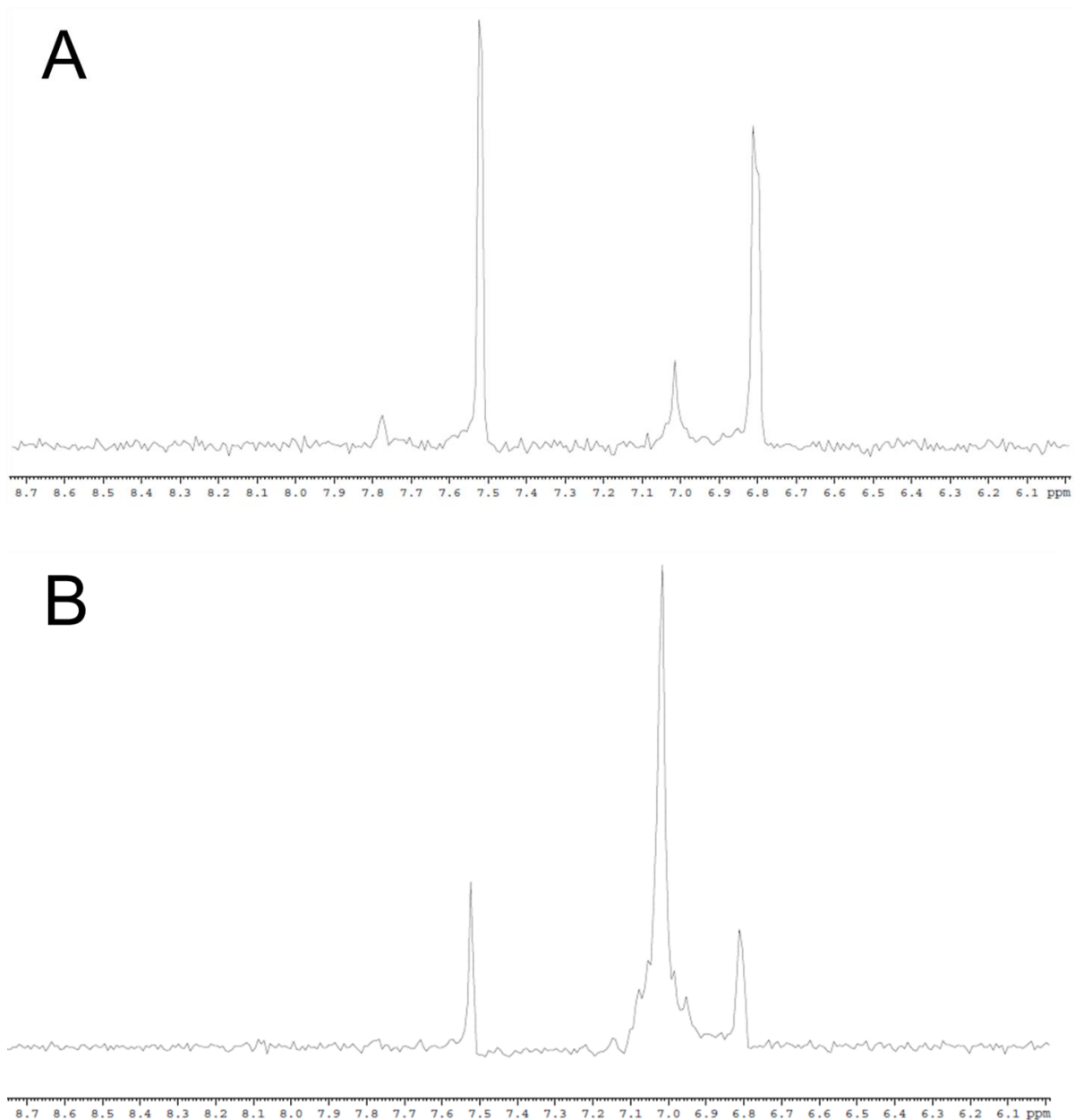
Figure 2.3 1D HSQC NMR spectra for incubated ^{15}N glutamine media (panel A) and incubated ^{15}N glutamine media with ^{15}N ammonium spike-in (panel B).

X-axes represent chemical shift in ppm with ^{15}N ammonium at 7.01 ppm and ^{15}N glutamine at 7.52 and 6.81 ppm. Media was incubated for 24 hours and NMR samples were in 10% D_2O. Incubated media samples contained 2 mM 2-^{15}N glutamine and the ^{15}N ammonium spike in contained 5 mM NH_4.

2.3.6 Dual isotope tracing and kinetic flux profiling in an extracellular flux assay

Analysis of glutamine metabolic pathway intermediates will allow for measuring mitochondrial health and function. A multichannel labelling (MCL) approach using dual stable isotope (^{13}C and ^{15}N) - labelled glutamine was applied to the *in vitro* fibroblast-based model. MCL inferred mitochondrial glutamine metabolic flux through quantifying labelled secreted extracellular metabolites derived from glutamine.

Fibroblasts were seeded in tissue culture treated 24 well plates at 5.0×10^4 live cells seeding density and allowed to grow for 24 hours. At t=0 h, the ^{12}C maintenance DMEM was aspirated off, cells were washed with 1 mL PBS, and the labelled DMEM was added with a working volume of 0.5 mL. Extracellular metabolite medium extractions were taken at t=48 h from cell culture medium and diluted 20-fold in 50% methanol. 50% methanol stabilizes polar metabolites and quenches any residual metabolism (Kostidis et al. 2017). Metabolic extractions were stored at -80°C until MS analysis. Metabolite extracts were ran on both RPIP and HILIC methods to detect and quantify TCA cycle metabolites and amino acids respectively, as described in Chapter 2.3.2 and 2.3.3. Kinetic flux profiling was conducted using extracellular carbon flux percentages, which were calculated using the following equation:

$$C\ flux\ \% = \frac{[13C\ labelled\ metabolite]}{[13C\ labelled\ nutrient\ uptaken]} x \frac{\#\ of\ 13C\ carbons\ in\ metabolite}{\#\ of\ 13C\ carbons\ in\ nutrient} x\ 100\%$$

For example, cells that consumed 500 µM of 5-^{13}C labelled glutamine nutrient and produced 100 µM of 5-^{13}C labelled glutamate metabolite dedicated 20% of carbon derived from 5-^{13}C glutamine to 5-^{13}C glutamate production.

Secreted metabolite concentrations present in biological samples were determined using external standard curves. Data were presented as mean ± standard error of the mean (SEM),

and assessed by Student's two-tailed t-tests and one-way ANOVA. P values < 0.05 were considered to be statistically significant.

2.3.7 Intracellular isotope enrichment assay

In addition to the extracellular assay, intracellular carbon isotope enrichment profiles of TCA cycle metabolites were determined to measure cellular carbon usage. Fibroblasts were seeded at 1.0×10^6 live cells seeding density into tissue culture treated T75 flasks, and allowed to grow to confluency for 24 hours. At t=0, cells were washed with 10 mL PBS and ^{13}C-labelled DMEM was added with a working volume of 10 mL. At t=72, DMEM was collected for extracellular metabolite quantification, and the PBS wash was repeated and fresh ^{13}C-labelled DMEM was added for a second t=0. This second incubation in labelled medium ensured steady state (i.e., non-changing over time) labelling to deduce partitioning of glutamine-derived carbon into downstream metabolites (Buescher et al. 2015). At t=24, cells were placed on an ice slurry and DMEM was collected for extracellular metabolite and ammonium quantification. Residual DMEM was aspirated off and intracellular metabolites were extracted using 7 mL cold 90% methanol added to the adherent cells, sitting on the ice slurry for 5 minutes with occasional swirling. Methanol allows for adequate intracellular metabolite extraction and stabilizes compounds to prevent interconversion (Lu et al. 2017). The methanol was then evaporated in a SpeedVac to 14x concentrate intracellular metabolites, which were then resuspended in 50% methanol for MS analysis.

All ^{13}C isotopomer peaks for each TCA cycle-associated metabolite were picked in MAVEN. Isotopomer ratio analysis calculated intracellular isotope enrichment percentages for intracellular metabolites using the following equation:

$$\textit{Isotope enrichment } \% = \frac{\textit{isotopomer signal intensity}}{\sum \textit{all isotopomers signal intensities}} \times 100\%$$

This percentage indicates metabolic flux through pathways that generate specific isotope labelling patterns based on the mitochondrial metabolic reactions that took place. Expected labelling patterns that arise from deficiencies in mitochondrial function are discussed in Chapter 1.3. Namely, cells with deficiencies in ETC function will have altered labelling patterns of glutamate, α-KG, and TCA cycle intermediates downstream of this.

2.4 Results

2.4.1 Detection and accurate quantification of TCA cycle metabolites

Solvent yielding optimal ionization of TCA cycle compounds and therefore highest MS signal intensities was found to be acetonitrile at pH 7.5 (Figure 2.4). This pH value is at least 2 points above the highest pKa of the TCA cycle metabolites being analyzed (PubChem), which ensures that metabolites in the column are negatively charged and will retain and separate on the column (Lu et al. 2017).

The standard curves generated for lactate, pyruvate, malate, fumarate, citrate, isocitrate, α-KG, and succinate were reproducible and above the sensitivity threshold. The accurate linear range for quantification was determined to be 5 µM to 100 µM and was used to quantify *in vitro* samples (Figure 2.5).
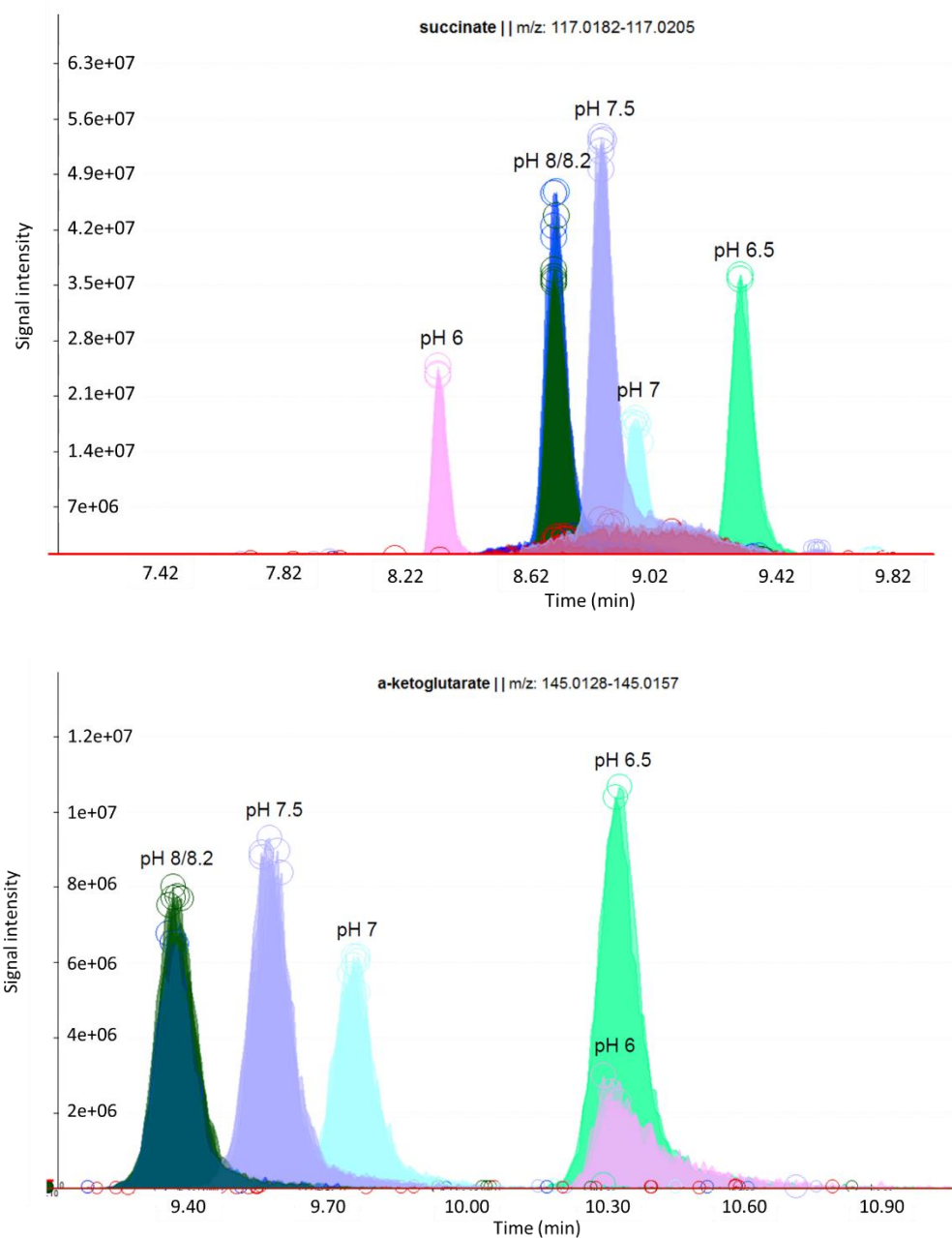
Figure 2.4 Extracted ion chromatograms (EICs) for succinate and α-KG.

Peaks represent signal intensities of succinate or α-KG at different pH values of RPIP solvent A.

X-axes represent retention times on RPIP LC in minutes and y-axes represent MS signal

intensities. m/z represents mass over charge ratio of metabolite. EICs were obtained using

Metabolomic analysis and visualization engine (MAVEN) software (Melamud et al. 2010).
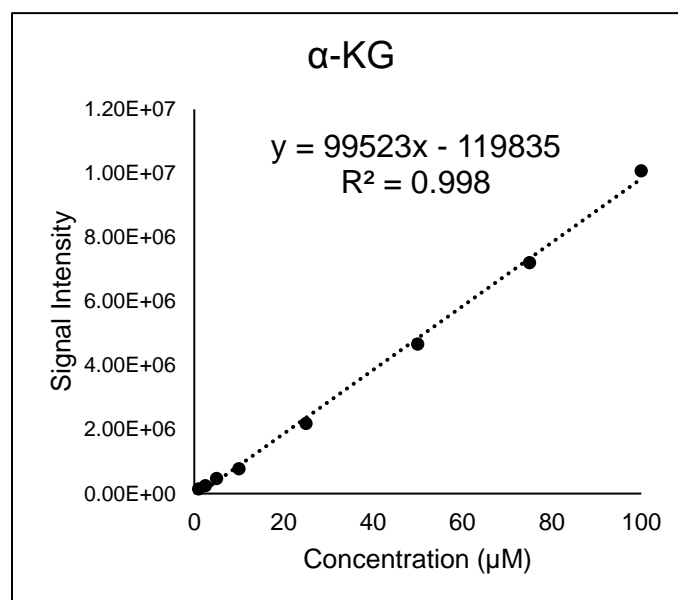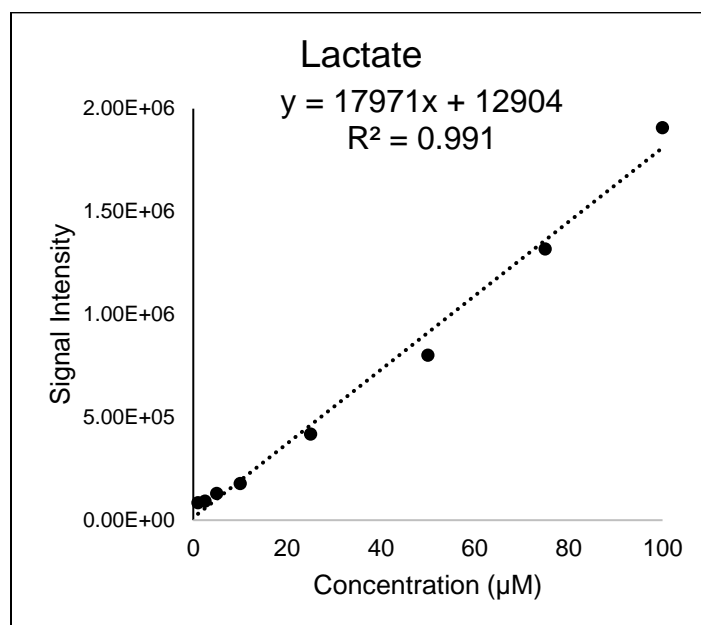
Figure 2.5 Standard curves for lactate and α-KG.

The line equations for quantification and R^2 values are shown at the top of each curve.

Standards were prepared in a DMEM + 10% dialyzed FBS matrix diluted 20-fold into 50%

methanol and run on the modified 15 minute RPIP method.

2.4.2 Detection and accurate quantification of amino acids and glucose

Standard curves generated of glucose, glutamate, glutamine, aspartate, asparagine, and alanine were reproducible and above the sensitivity threshold. The accurate linear range for quantification was determined to be 5 µM to 100 µM and was used to quantify *in vitro* samples (Figure 2.6).
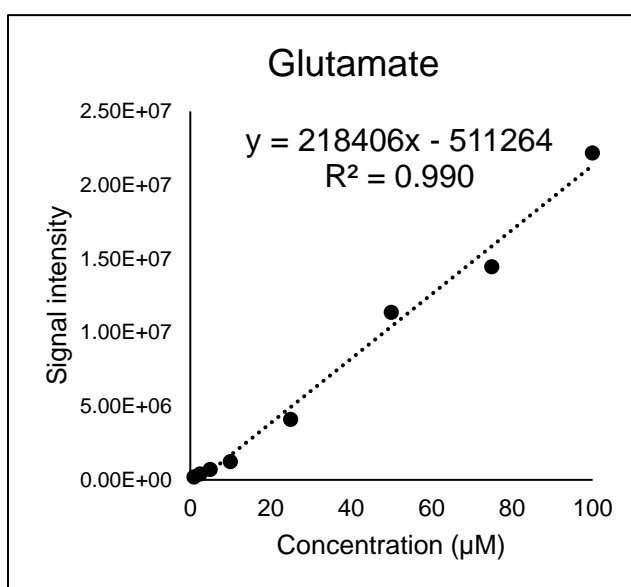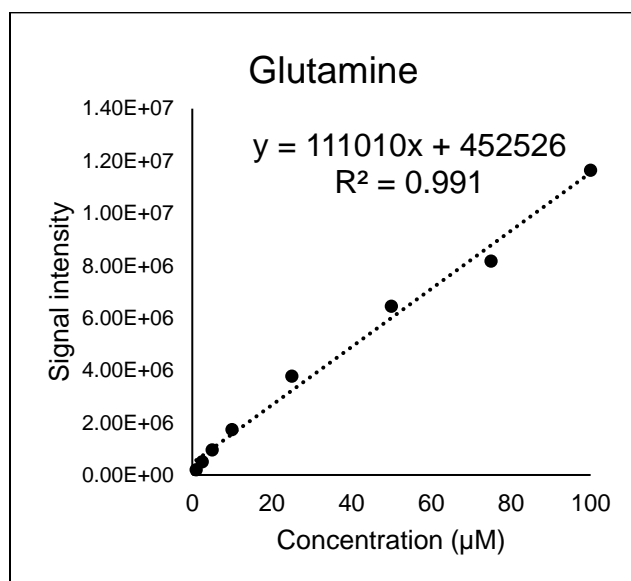
Figure 2.6 Standard curves for glutamine and glutamate.

The line equations for quantification and R^2 values are shown at the top of each curve.

Standards were prepared in a DMEM + 10% dialyzed FBS matrix diluted 20-fold into 50%

methanol and run on the 5 minute HILIC method.

2.4.3 Detection and accurate quantification of ammonium ions

Proton 1D ^{1}H ^{15}N HSQC NMR specifically detected and quantified glutamine-derived ammonium, as was traced by the ^{15}N label. The standard curve generated for ^{15}N ammonium was reproducible and above the sensitivity threshold. The accurate linear range for quantification was determined to be 150 μM to 750 μM and was used to quantify *in vitro* samples (Figure 2.7).
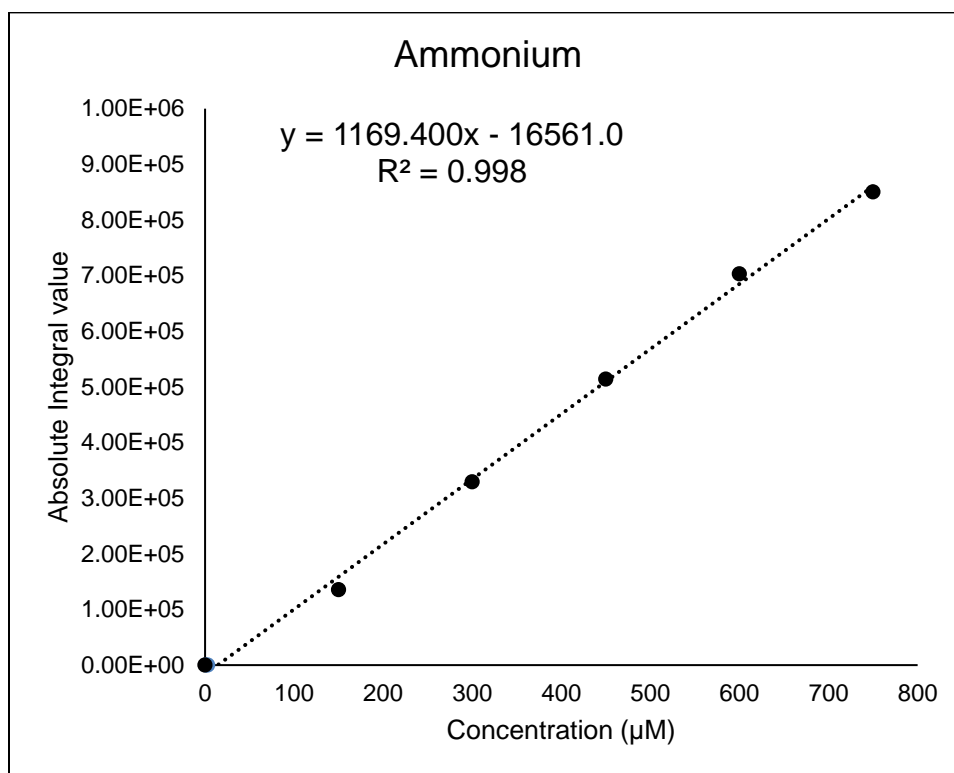
Figure 2.7 Standard curve for ^{15}N NH$_4$Cl using 1D HSQC NMR.

The line equations for quantification and R^2 values are shown at the top of the curve. Standards

were prepared in a DMEM + 10% dialyzed FBS matrix in 10% D$_2$O.

2.4.4 Intracellular isotope partitioning

Intracellular isotope enrichment percentages measured steady state labelling of TCA cycle metabolites and were calculated as described in Chapter 2.3.7. An example of an isotope enrichment profile is shown in Figure 2.8 for the α-KG isotopomers present in fibroblasts. Metabolite levels indicated by signal intensity differ from the isotope enrichment profiles; levels indicate amount of metabolite consumed or produced in the extracellular fluid while isotope enrichment indicates intracellular carbon usage.
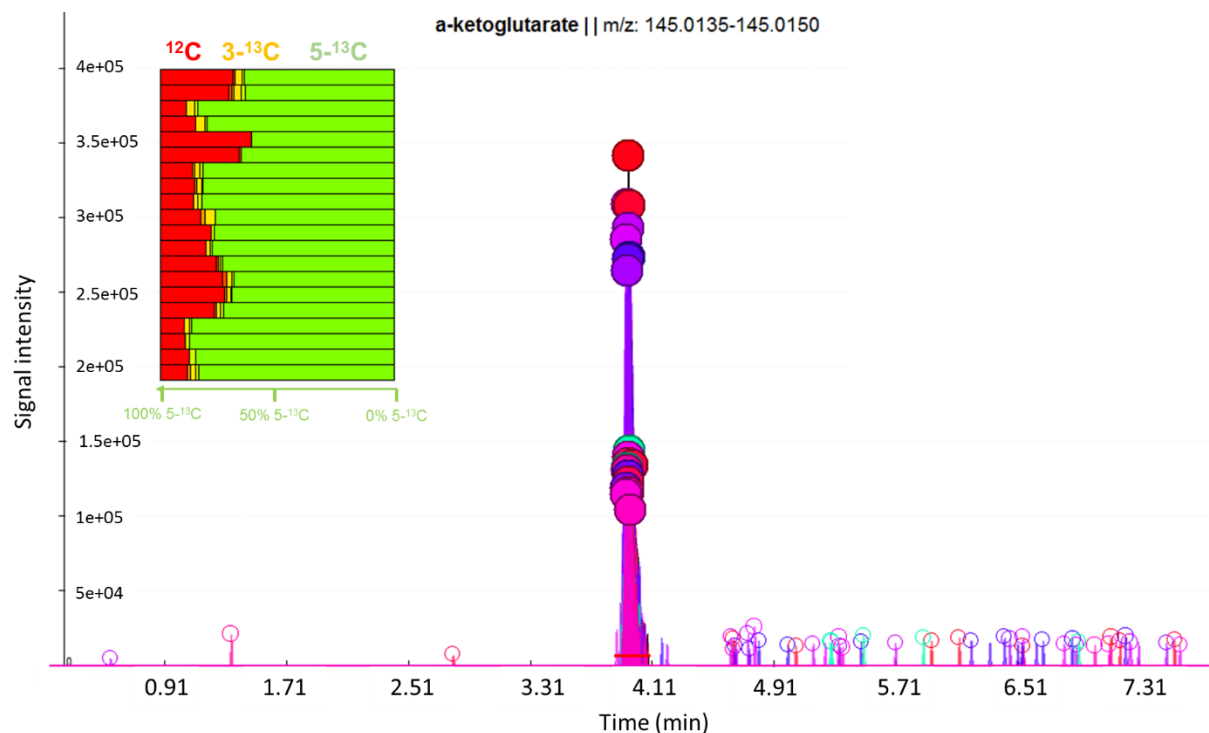
Figure 2.8 EIC with intracellular isotope enrichment profiles of α-KG in fibroblast samples.

Isotope enrichment percentages (left bar plot) are derived from the α-KG MS peak. Isotope enrichment percentages are shown as: ^{12}C α-KG in red, 3-^{13}C α-KG in yellow, and 5-^{13}C α-KG in green, with percentage of 5-^{13}C α-KG isotopomers shown below the bar plot for reference. Dermal fibroblasts were provided 5-^{13}C labelled glutamine in DMEM and incubated for 72 hours, then 24 hours. Intracellular metabolite extractions were run on a modified RPIP method (Lu et al. 2010). EIC was obtained using MAVEN software (Melamud et al. 2010).

2.5 Discussion

In this study, we present an analytical hybrid LC-MS/NMR approach using MCL to quantify

mitochondrial metabolism (Figure 2.9). Optimized chromatographic conditions allowed for the

detection and accurate quantification of various extracellular and intracellular mitochondrial

metabolism-associated metabolites. The NMR assay developed quantifies glutamine-derived

ammonium ions secreted by fibroblasts. This practical system uses fibroblast metabolite

extracts to measure glutamine metabolic flux and mitochondrial health.

While these methods developed yield an assessment of mitochondrial metabolism with

respect to glutamine catabolism, the methods developed do not measure other mitochondrial

metabolism pathways. Specifically, branched chain amino acids (leucine, isoleucine and valine),

and fatty acid catabolism. This is an important aspect to investigate to understand DCMA

because of the potential link between leucine catabolism and the 3-MGA-urias. The oxidation of

fatty acids provides up to 90% of cardiac tissue ATP and thus studying fatty acid catabolism

may present better insight into DCMA disease progression and heart failure (Doenst et al.

2013).

These methods also do not measure oxygen consumption and ATP production, which

represent direct measurements of oxidative metabolism; this cannot be directly achieved

through quantifying the rate of production of metabolites alone and requires more specific

methodologies. Moreover, positive ions present in biological samples (such as arginine) were

not detected because of the ion pairing agent TBA, used in the RPIP method. TBA suppresses

ionization and therefore detection of positively charged molecules (Lu et al. 2017). Another

limitation to these methods is that the accurate linear range of quantification for glucose and

lactate, on the HILIC and RPIP methods respectively, was determined to be 5 µM to 100 µM.

However, DMEM contains 25 mM glucose and after a 20-fold dilution into 50% MeOH during

MS sample preparation, the final concentration is 1250 µM. After incubation, fibroblasts are

expected to consume ~90% of this glucose and convert it to two lactate molecules per glucose molecule consumed (Tanner et al. 2018). This would theoretically be over 2000 µM lactate present in a metabolite extract. Thus, further dilutions beyond the initial 20-fold dilution are required for accurate glucose and lactate quantification.

Accurate detection and quantification of mitochondrial metabolism-associated compounds will allow for an indirect assessment of mitochondrial function and health. Glutamine is directly metabolized in the mitochondrion and measuring analytes associated with its catabolism presents a direct measurement of mitochondrial function. Namely, quantifying both carbon nutrients (glucose and glutamine) uptake and secreted glutamine-derived metabolites alongside isotope analysis assesses mitochondrial health in the fibroblast model system. This biochemical assay has applications for not only measuring mitochondrial glutamine metabolism in DCMA, but also can be applied to fibroblasts derived from patients with other mitochondrial diseases with known or unknown underlying disease mechanisms. This will characterize the metabolic consequences of inhibiting different aspects of mitochondrial metabolism.
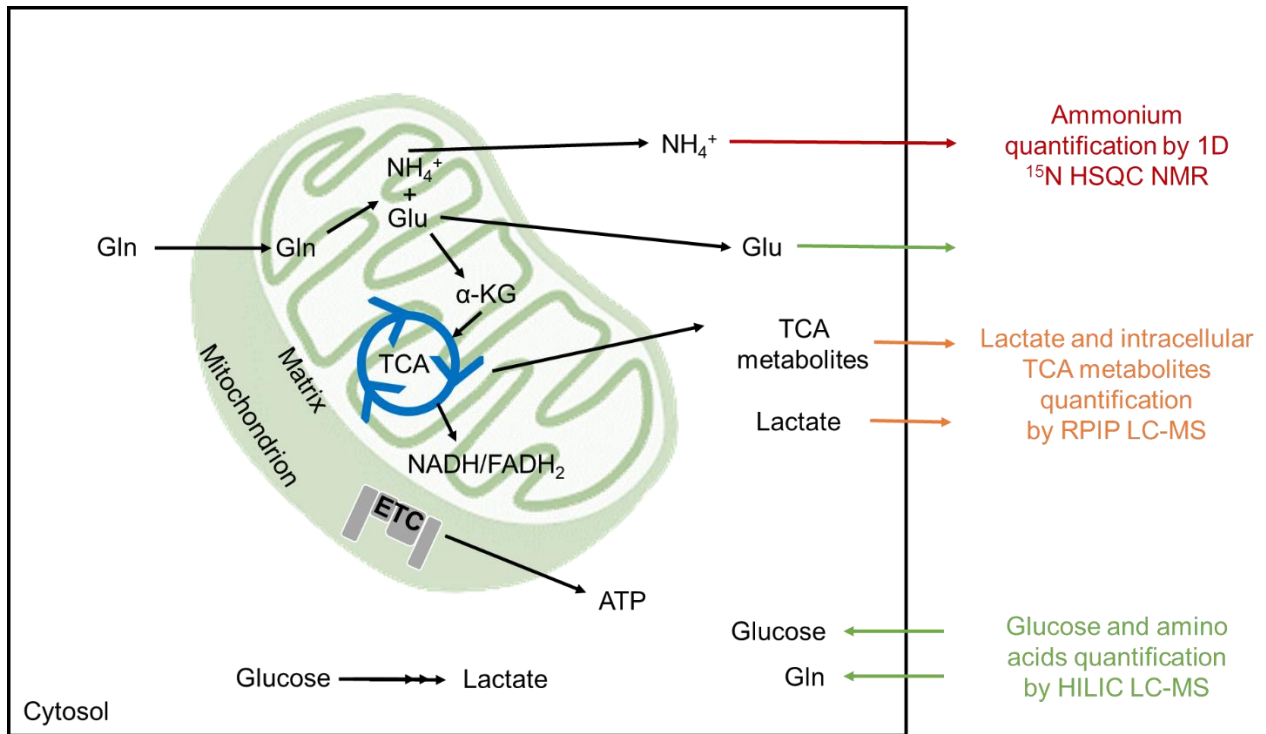
Figure 2.9 Analytical methods of LC-MS and NMR developed to quantify mitochondrial health in a fibroblast-based model system.

NMR detects and quantifies glutamine-derived ammonium ions, and LC-MS detects and quantifies glucose-derived lactate, glutamine-derived amino acids, and glutamine-derived TCA cycle metabolites.

Chapter Three: CHARACTERIZATION OF DCMA MITOCHONDRIAL METABOLISM

3.1 Abstract

Determination of mitochondrial health in DCMA cells will characterize the metabolic

consequences of a *DNAJC19* mutation. Previous DCMA studies have suggested some potential

underlying disease mechanisms to be related to mitochondrial function, yet overlook

mitochondrial metabolism. This study measured DCMA mitochondrial metabolism using the

methods developed in Chapter 2. Surprisingly, we did not observe the established DCMA

metabolic phenotype of 3-MGA and 3-MGC production. Instead, we identified a previously

undescribed DCMA metabolic phenotype: increased glutamine consumption, increased

glutamate and ammonium production, and decreased glutamine recycling, with implied normal

mitochondrial function in the context of TCA cycle metabolic flux. This novel finding introduces a

new element to the underlying disease mechanism and sheds new light on amino acid

metabolism in DCMA. In addition, this metabolic phenotype correlated with DCMA patient

outcomes. The biochemical assay was applied to a blinded cohort of DCMA-patient derived

fibroblasts of unknown disease severity and successfully predicted the outcome of eight patient

lines. This has applications to predict disease prognosis in DCMA patients to improve quality of

life.

3.2 Introduction

Previous DCMA studies overlooked mitochondrial metabolism yet investigated indirect

consequences of it, such as mitochondrial structure and patient outcomes (Davey et al. 2006;

Richter-Dennerlein et al. 2014). Applying metabolomics to DCMA will identify the specific direct

consequences of the *DNAJC19* mutation on mitochondrial metabolism and elucidate its role in

disease development. Currently, the DCMA metabolic phenotype consists of increased

production of 3-MGA and 3-MGC, which are elevated in patient urine, cerebrospinal fluid and

plasma. These organic acids have been suggested to be produced as a result of perturbed

mitochondrial function (Wortmann et al. 2012). Although diagnostic, levels of these acids do not

correlate with disease progression in DCMA patients (Davey et al. 2006). Furthermore, although

metabolism is the primary feature used to diagnose DCMA, primarily non-metabolic hypotheses

have emerged to explain the clinical progression of this disease (Davey et al. 2006; Richter-

Dennerlein et al. 2014; Wortmann et al. 2012). Surprisingly, hypotheses regarding the

underlying mechanism in DCMA do not include the diagnostic elevated levels of 3-MGA and 3-

MGC which suggest perturbed mitochondrial function.

The analytical methods adapted and optimized in Chapter 2 specifically target glutamine

metabolism to assess mitochondrial metabolism and function. In addition to these novel tools, I

have access to a unique collection of DCMA patient-derived dermal fibroblasts with clinical

phenotypes ranging from mild to severe cardiac dysfunction. Dermal fibroblasts are derived

from patient skin biopsies, which are a standard clinical procedure (Vangipuram et al. 2013). **We

quantified cellular perturbations in fibroblasts derived from DCMA patients with mild or

severe disease severity with the objective of assessing DCMA fibroblast glutamine

metabolism.** We also applied our analysis to a series of blinded patient fibroblasts to correlate

disrupted mitochondrial function with patient clinical phenotype in an attempt to develop a novel

prognostic clinical assay.

The first reaction of the glutamine catabolic pathway is the mitochondrial matrix

glutaminase reaction (Gross et al. 2014). Glutamine metabolism is known to be affected by

deficiencies in mitochondrial function due to their direct links: glutamine is the primary

contributor to the TCA cycle which produces reducing equivalents that deposit their electrons at

the ETC for mitochondrial respiration (Chen et al. 2018). Glutaminase is the first reaction in the

glutamine catabolic pathway. This reaction hydrolyzes ammonium off the side chain of

glutamine, producing glutamate and ammonium. This ammonium is incorporated into the urea

cycle or is excreted out of the cell (Foschi et al. 2015). Inhibiting the glutaminase reaction in DCMA fibroblasts should have a measurable metabolic effect if this is indeed the increased metabolic flux in DCMA. A potent, reversible glutaminase inhibitor, CB-839, which noncompetitively inhibits glutaminase, was applied to the model system to investigate its ties to the DCMA metabolic mechanism (Gross et al. 2014).

3.3 Methods and Materials

The extracellular flux assay described in Chapter 2.3.6 was used to quantify mitochondrial metabolism in DCMA patient-derived dermal fibroblasts. In addition to this, the intracellular isotope enrichment assay described in Chapter 2.3.7 was used to assess DCMA mitochondrial carbon flux and overall health.

The flux assay (Chapter 2.3.6) was also applied to a cohort of cell lines derived from DCMA patients with unknown disease severity in a blinded trial to develop a potential novel clinical diagnostic tool. A severity threshold using biomarker concentrations was determined to predict DCMA patient outcomes. Predictions were confirmed by comparisons to the clinical data available on patients for which these cell lines were derived. Cell lines were determined to be either mild (mild cardiac dysfunction DCMA) or severe cardiac dysfunction based on a heuristic algorithm. This algorithm determined if a cell line was within the standard deviation of being classified as mild or severe DCMA using secreted biomarker concentrations. The z score for each blinded cell line was determined using the mild DCMA population biomarker concentration average and standard deviation values. From the z score, cell lines were predicted to be within the mild DCMA population or not (thus would be predicted as severe). Negative and positive control cell lines were also run to test the accuracy of the assay.

Glutaminase inhibitor CB-839 was dissolved in 0.1% DMSO to give a final concentration of 0.1 µM in isotope-labelled DMEM (MCL described in Chapter 2.3.6). The effects of CB-839

treatment on one severe DCMA fibroblast cell line and two control cell lines were measured

using the established extracellular metabolic flux assay (Chapter 2).

3.4 Results

3.4.1 DCMA fibroblasts did not demonstrate the expected metabolic phenotype

First, the diagnostic biomarkers for DCMA of 3-MGA and 3-MGC production were looked for in the fibroblast model system. However, this phenotype was not exhibited in DCMA fibroblasts. Fibroblast medium sample signal intensities for these compounds were within noise signals of 3-MGA and 3-MGC, indicating their absence (Figure 3.1 for 3-MGC, and 3-MGA followed the same pattern).
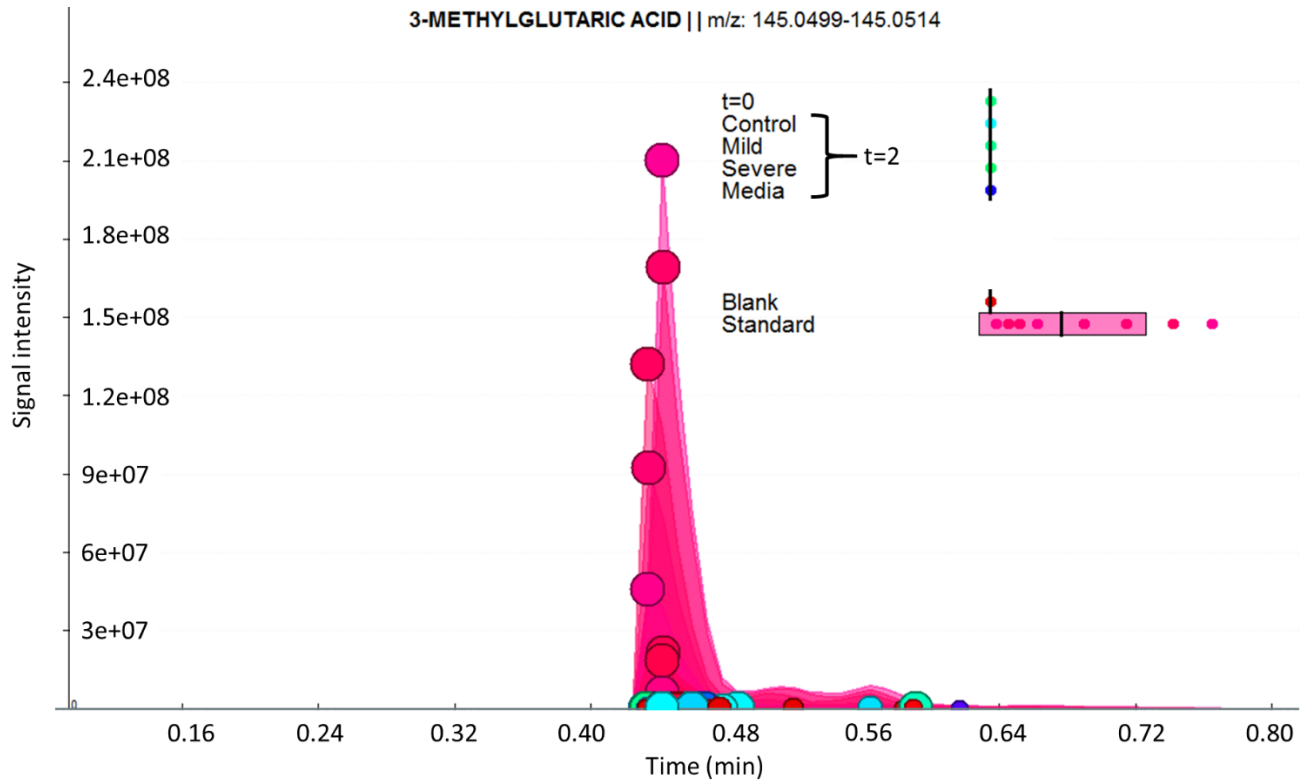
Figure 3.1 3-MGA EIC from dermal fibroblasts.

X-axis represents retention times in minutes on HILIC LC and y-axis represents MS signal intensities. The EIC shows peaks of 3-methylglutaric acid standard samples in pink, and the biological or blank samples in other colours. Samples from top to bottom represented as bar plots are: t=0 represents fibroblast medium after 0 hours incubation; Control, Mild, or Severe t=2 represents control or DCMA (Mild or Severe cardiac dysfunction) fibroblast medium after 48 hours incubation; Media t=2 represents medium containing no cells after 48 hours incubation; Blank represents blank MS injection of 50% methanol. These data are the individual points of nine cell lines with three separate technical replicates for a total of 27 MS peaks per condition. m/z represents mass over charge ratio of metabolite. EIC was obtained using MAVEN software (Melamud et al. 2010).

3.4.2 A novel DCMA phenotype: altered glutamine metabolism

As previously discussed, direct measurement of glutamine metabolism gives an assessment of mitochondrial function and health. An MCL approach using dual isotope-labelled glutamine was used to study the glutamine metabolic flux of DCMA fibroblasts. DCMA fibroblasts exhibited increased glutamine nutrient consumption compared to control fibroblasts. This phenotype did not correlate with disease severity but, as seen in Figure 3.2, DCMA fibroblasts consumed significantly more glutamine compared to controls.

DCMA fibroblasts also exhibited significantly increased glutamine-derived glutamate production (Figure 3.3). This metabolic phenotype also did not correlate with disease severity, and thus these glutamate biomarkers were omitted from the development of the predictive assay. Normally, fibroblasts partially catabolize glutamine into downstream metabolites which can undergo reverse reactions to re-produce glutamine. This glutamine recycling metabolic phenotype was dramatically decreased in DCMA and correlated with disease severity, making $5\text{-}^{13}C$ $1\text{-}^{15}N$ and $5\text{-}^{13}C$ glutamine production good biomarkers for the predictive assay (Figure 3.4). Moreover, the observed DCMA metabolic phenotypes were not affected by availability of glucose (Figure 3.5), or oxygen (Figure 3.6). Fibroblasts were provided 5.5 mM glucose initially, and at the time of metabolite extraction, over 90% of the glucose was consumed. To control for this, the effects of varying glucose concentrations on the metabolic phenotype were measured and were found to persist despite varying glucose concentrations. Also, the oxygen availability in a 24 well tissue culture plate was not measured, as this can directly affect mitochondrial metabolism. To control for this, the effects of varying oxygen concentrations on the metabolic phenotype were measured and found to persist despite varying oxygen concentrations. This indicates that the observed DCMA metabolic phenotype is not due to limiting glucose or oxygen conditions, but rather due to the underlying *DNAJC19* mutation.

DCMA fibroblasts produced more glutamine-derived ammonium ions, which were excreted into the extracellular fluid alongside the observed carbon metabolites (Figure 3.7). These are glutamine-derived as they carry the ^{15}N stable isotope label. The MED bar represents ^{15}N ammonium levels present in incubated media, indicating that there is normal degradation of ^{15}N glutamine to ^{15}N ammonium (detected by NMR). However, the spent fibroblast medium ^{15}N ammonium levels are significantly higher indicating that the ammonium ions detected are derived from biological reactions, and not due to sample degradation.
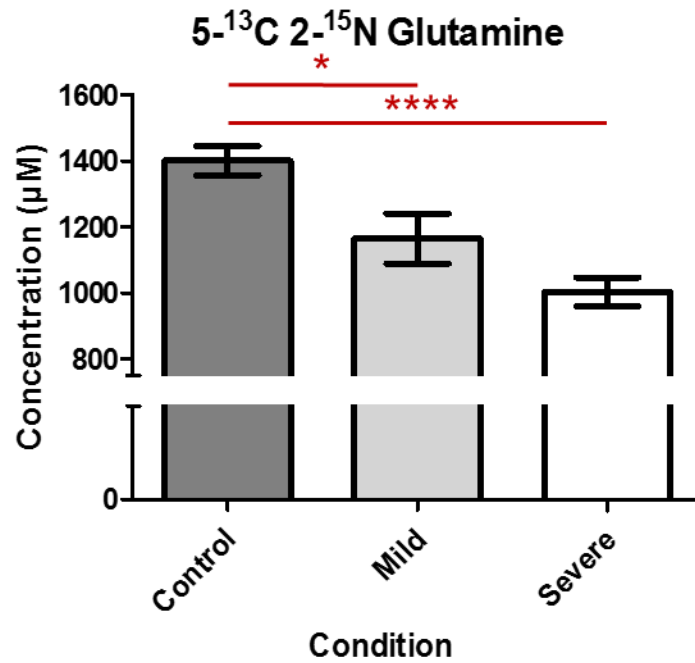
Figure 3.2 Dual stable isotope-labelled glutamine uptake from DMEM by fibroblasts.

Glutamine concentration (µM) in fibroblast medium after 48 hours incubation. Dermal fibroblasts from controls and DCMA patients with mild and severe cardiac dysfunction were provided 5-^{13}C 2-^{15}N stable isotope-labelled glutamine in DMEM. These data represent the average of three biological replicates per condition, with three separate technical replicates. Bars represent ± SEM of 27 replicates, and * represents $p < 0.05$ and **** $p < 0.0001$ using Student's two-tailed t-test.

Figure 3.3 Labelled glutamine-derived glutamate production by fibroblasts.

5-13C 1-15N and 5-13C labelled glutamate concentration (µM) in fibroblast medium after 48 hours incubation with 15N isotope or unlabelled N. Dermal fibroblasts from controls and DCMA patients with mild and severe cardiac dysfunction were provided 5-13C 2-15N stable isotope-labelled glutamine in DMEM. These data are the average of three biological replicates per condition, with three separate technical replicates. Bars represent ± SEM of nine replicates, and *** represents $p < 0.0005$ and **** $p < 0.0001$ using Student's two-tailed t-test.
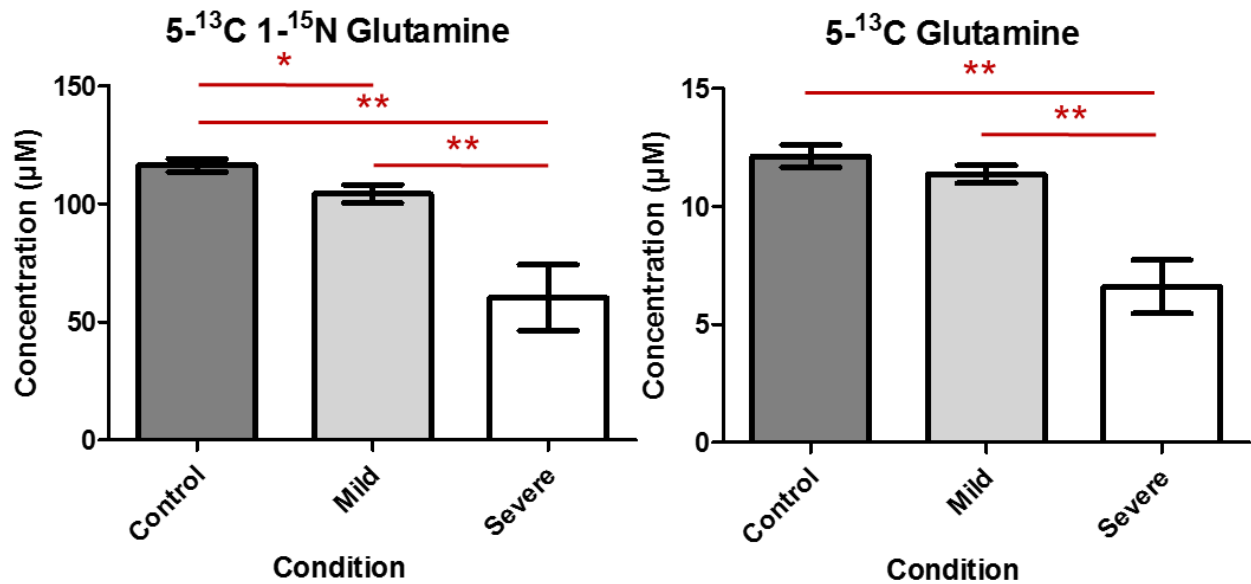
Figure 3.4 Glutamine isotopomer production (glutamine recycling) by fibroblasts.

$5\text{-}^{13}C$ $1\text{-}^{15}N$ and $5\text{-}^{13}C$ labelled glutamine concentration (μM) in fibroblast medium after 48 hours incubation. Dermal fibroblasts from controls and DCMA patients with mild and severe cardiac dysfunction were provided $5\text{-}^{13}C$ $2\text{-}^{15}N$ stable isotope-labelled glutamine in DMEM. These data are the average of three biological replicates per condition, with three separate technical replicates. Bars represent ± SEM of nine replicates, and * represents $p < 0.05$ and ** $p < 0.005$ using Student's two-tailed t-test.

5-^{13}C 1-^{15}N glutamine

5-^{13}C glutamine

5-^{13}C 1-^{15}N glutamate
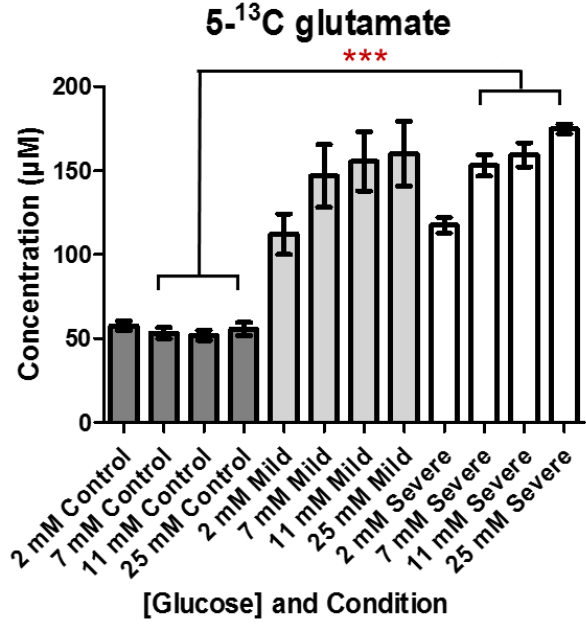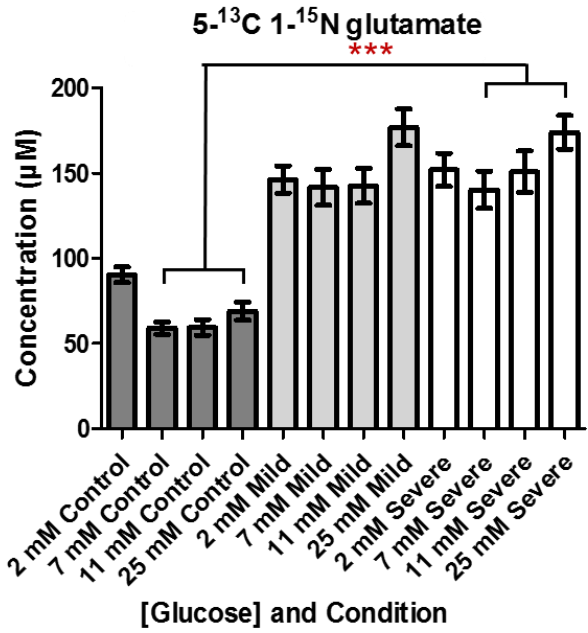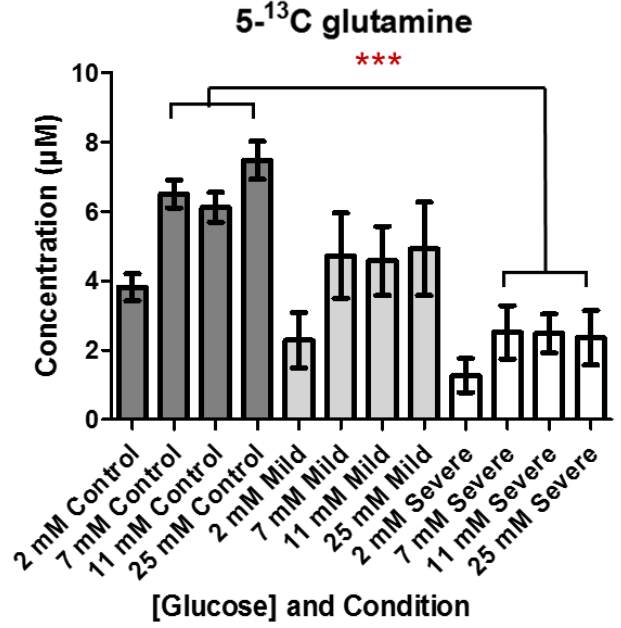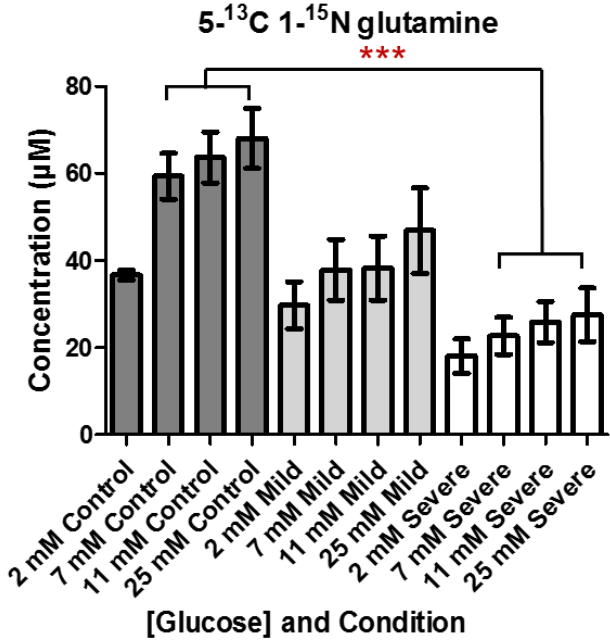
5-^{13}C glutamate

Figure 3.5 Glutamine and glutamate production by fibroblasts at different glucose concentrations.

5-^{13}C 1-^{15}N and 5-^{13}C labelled glutamine and glutamate concentrations (µM) in fibroblast medium after 48 hours incubation at varying glucose concentrations from 2 mM (low or 'hypoglycemic') to 25 mM (high or 'hyperglycemic'). Dermal fibroblasts from controls and DCMA patients with mild and severe cardiac dysfunction were provided 5-^{13}C 2-^{15}N stable isotope-labelled glutamine in DMEM. These data are the average of three biological replicates per condition, with three separate technical replicates. Bars represent ± SEM of nine replicates, and *** represents $p < 0.0005$ using one-way ANOVA. No significant differences were observed between the 7-25 mM glucose concentrations within each condition.

5-^{13}C 1-^{15}N glutamine

5-^{13}C glutamine

5-^{13}C 1-^{15}N Glutamate
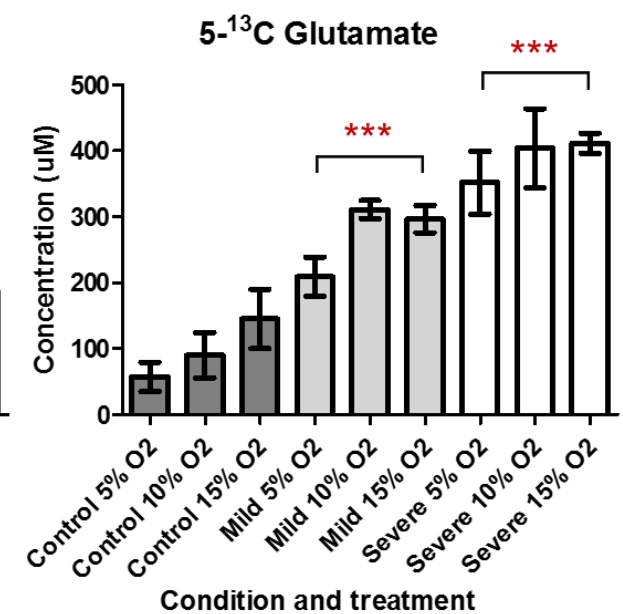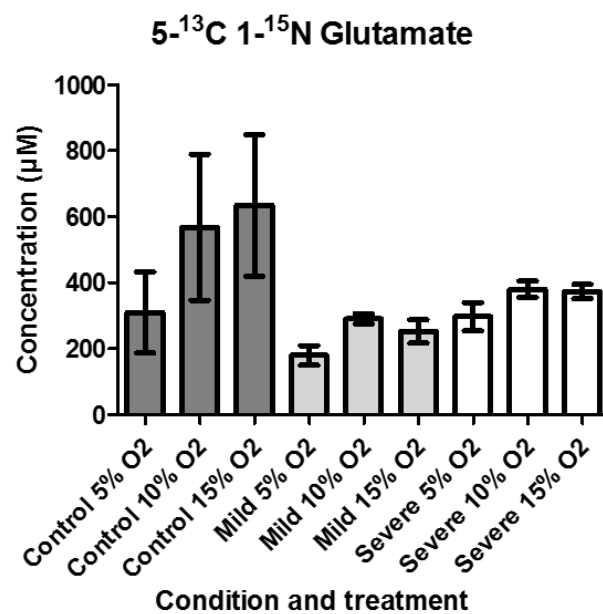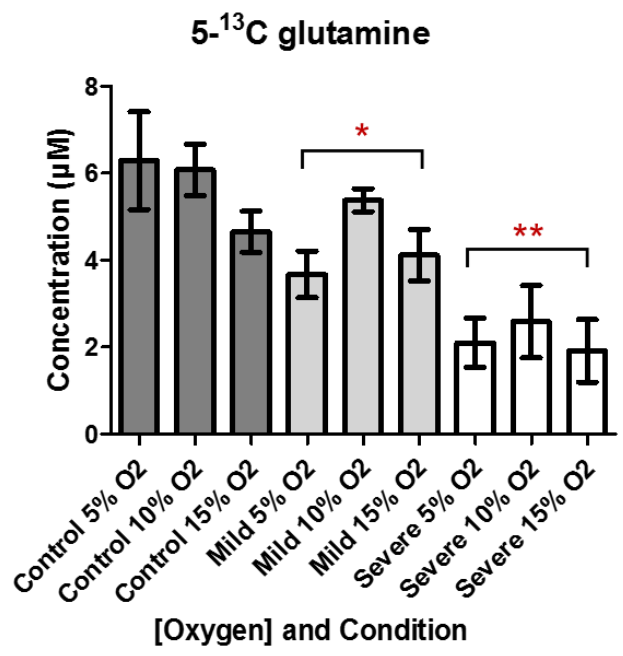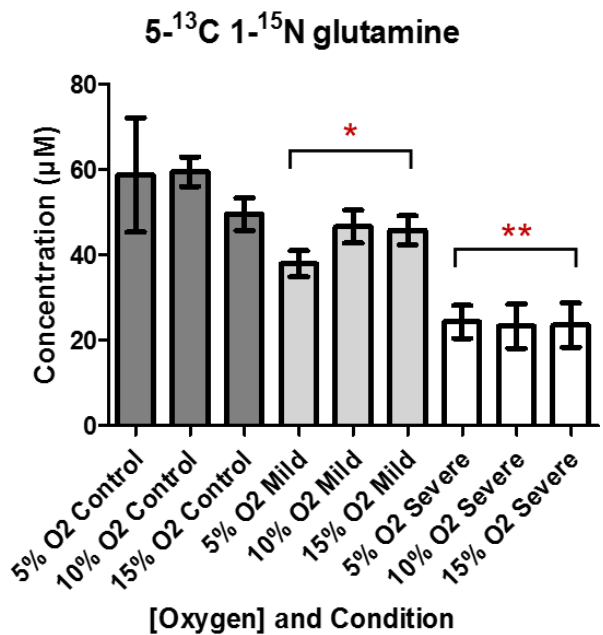
5-^{13}C Glutamate

Figure 3.6 Glutamine and glutamate production by fibroblasts at different oxygen concentrations.

$5\text{-}^{13}C$ $1\text{-}^{15}N$ and $5\text{-}^{13}C$ labelled glutamine and glutamate concentrations (µM) in fibroblast medium after 24 hours incubation at varying oxygen concentrations from 5% (low or 'hypoxic') to 15% (high or 'hyperoxic'). Dermal fibroblasts from controls and DCMA patients with mild and severe cardiac dysfunction were provided $5\text{-}^{13}C$ $2\text{-}^{15}N$ stable isotope-labelled glutamine in DMEM. These data are the average of three biological replicates per condition, with three separate technical replicates. Bars represent ±SEM of nine replicates, and * represents $p < 0.05$ and ** $p < 0.005$ using one-way ANOVA. No significant differences were observed between the 5-15% O_2 concentrations within each condition.
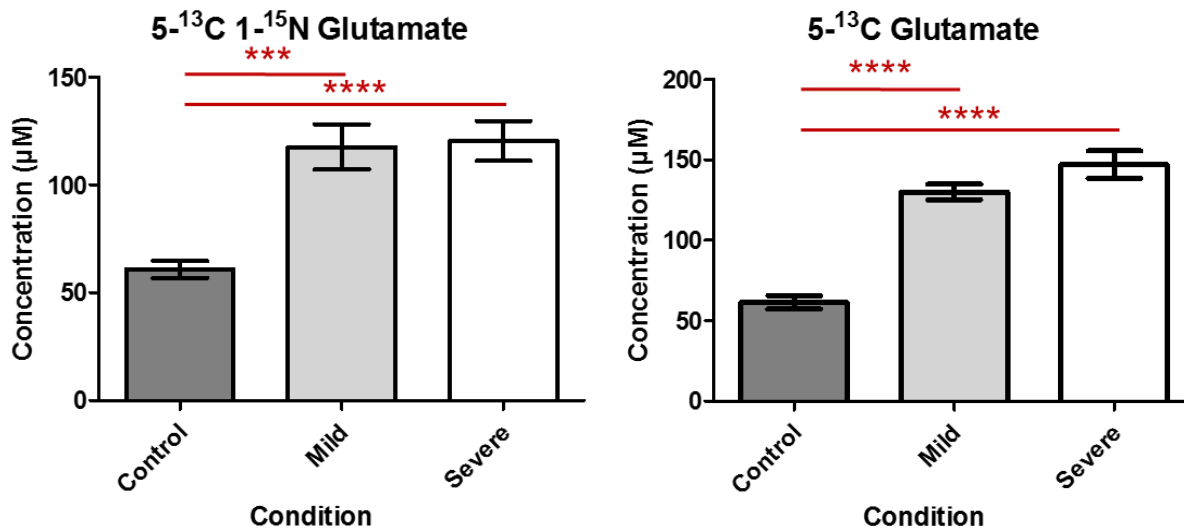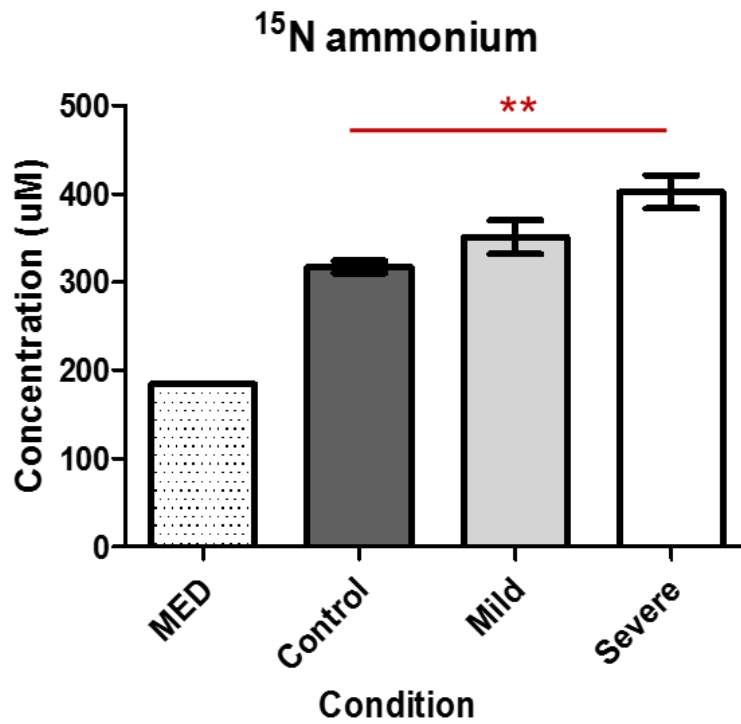
Figure 3.7 [15]Nitrogen labelled ammonium production by fibroblasts.

[15]N-labelled ammonium concentration (μM) in fibroblast medium after 24 hours incubation. Dermal fibroblasts from controls and DCMA patients with mild and severe cardiac dysfunction were provided 5-[13]C 2-^{15}N stable isotope-labelled glutamine in DMEM, and labelled DMEM was incubated (MED). These data are the average of three biological replicates per condition, with two separate technical replicates. Bars represent ±SEM of six replicates and ** represents $p < 0.005$ using Student's two-tailed t-test.

*3.4.3 Glutamine carbon flux in extracellular ^{13}C metabolites*

To measure the amount of glutamine carbon dedicated to secreted metabolites, carbon flux percentages were calculated using concentration of labelled metabolite over concentration of dual-labelled glutamine consumed by fibroblasts.

The carbon fluxes of 5-^{13}C 1-^{15}N and 5-^{13}C isotopomers of glutamine and glutamate are shown in Figure 3.8. Severe DCMA fibroblasts dedicated ~15% less carbon to glutamine recycling and ~6% more carbon to glutamate production, while mild DCMA fibroblasts dedicated ~8% less carbon to glutamine recycling and ~9% more carbon to glutamate production. These differences demonstrate the decreased glutamine recycling and increased glutamate production metabolic fluxes in DCMA.
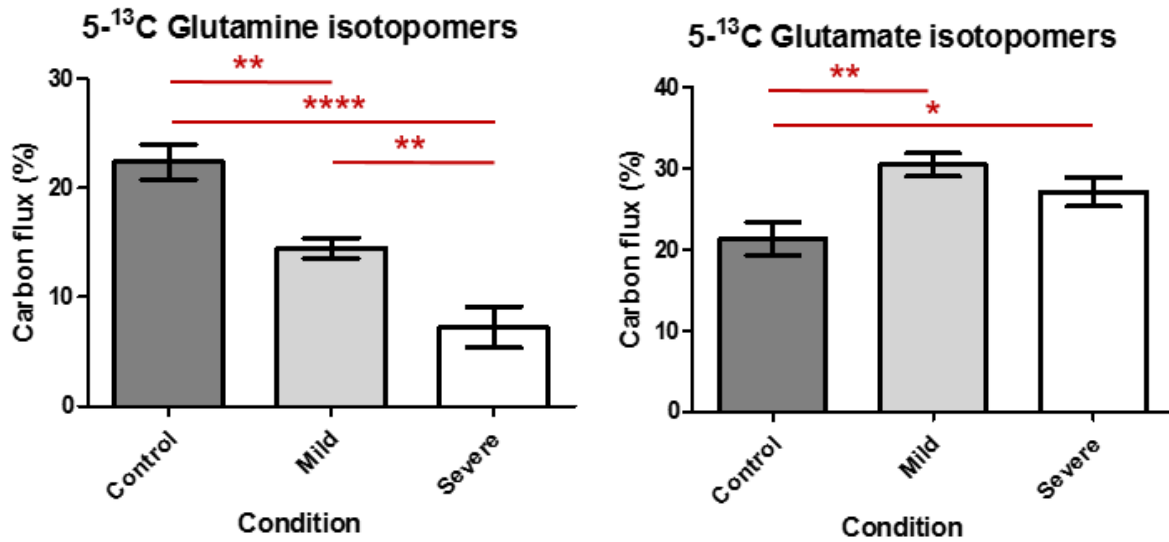
Figure 3.8 ^{13}C extracellular glutamine and glutamate carbon flux balance analysis by fibroblasts.

Percentage of carbon flux dedicated to 5-^{13}C glutamine (left) and glutamate (right) isotopomers production in fibroblast medium after 48 hours incubation. Flux is the sum of percentages of both 5-^{13}C 1-^{15}N and 5-^{13}C glutamine and glutamate isotopomers. Dermal fibroblasts from controls and DCMA patients with mild and severe cardiac dysfunction were provided 5-^{13}C 2-^{15}N stable isotope-labelled glutamine in DMEM. These data are the average of three biological replicates per condition, with three separate technical replicates. Bars represent ± SEM of nine replicates, and * represents $p < 0.05$, ** $p < 0.005$, and **** $p < 0.0001$ using Student's two-tailed t-test.

3.4.4 DCMA exhibits normal LDH flux

Glucose-derived lactate production was measured in fibroblasts to determine if the LDH electron dumping reaction rates were increased in DCMA. Glucose consumption was increased in severe DCMA fibroblasts; however, lactate production was not different between control and DCMA fibroblasts (Figure 3.9). Severe DCMA fibroblasts took up 5.11 mM glucose and produced 12.5 mM lactate, and control fibroblasts took up 3.99 mM glucose and produced 11.0 mM lactate. Normally, one glucose molecule breaks down into two lactate molecules giving an expected 1:2 ratio of glucose:lactate (Tanner et al. 2018). However, lactate can be derived from other sources such as alanine deamination into pyruvate via ALT, and reduction to lactate in the LDH reaction, resulting in the observed deviations from the expected 1:2 ratio (Conway 2011).

3.4.5 DCMA exhibits normal mitochondrial carbon flux

Isotope enrichment percentages were calculated for DCMA fibroblasts at steady state labelling in 5-^{13}C glutamine to measure intracellular carbon usage. Surprisingly, intracellular labelling profiles between all nine fibroblast cell lines consisting of dermal fibroblasts from controls and DCMA patients with mild and severe cardiac dysfunction were not significantly different in any of the TCA cycle metabolites or aspartate (Figure 3.10). In fibroblasts, most (~70%) of the steady state TCA cycle carbon is derived from glutamine (initially supplied with 2 mM), indicating that this was the major contributor to the TCA cycle rather than glucose carbon (initially supplied with 5.5 mM). +5 α-KG undergoes mitochondrial oxidative TCA cycle turning to produce +4 labelled isotopomers of downstream metabolites up to aspartate. Alternatively, +5 α-KG can be exported out into the cytosol to under reductive carboxylation to produce +5 citrate. This +5 citrate molecule undergoes the ATP-citrate lyase reaction to produce +2 acetyl-CoA and +3 oxaloacetate (Mullen et al. 2012). +3 oxaloacetate then can undergo the reversible cytosolic malate dehydrogenase reaction to produce +3 malate, enter the mitochondrion and

undergo the reverse fumarase reaction to produce +3 fumarate (Mullen et al. 2012; Mescam et al. 2011). +3 oxaloacetate can also be imported into the mitochondria where it is transaminated via the AST reaction to produce +3 aspartate (Conway 2011). These various mechanisms produce the observed isotope enrichment profiles of normal fibroblasts, which did not differ in mild or severe DCMA fibroblasts.
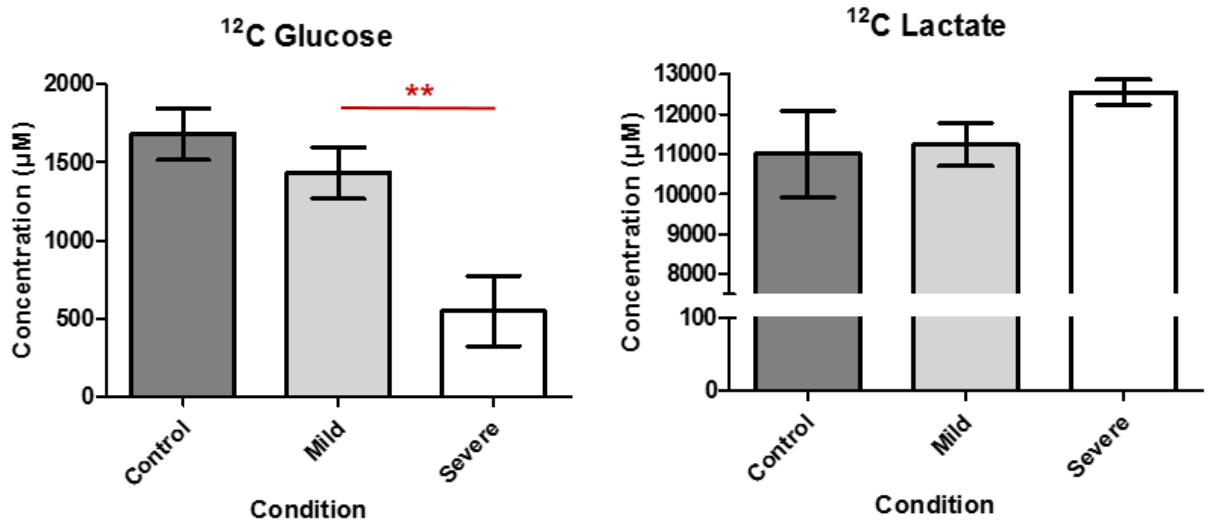
Figure 3.9 Normal glucose metabolism by DCMA fibroblasts.

Glucose and lactate concentrations (µM) in fibroblast medium after 48 hours incubation. Dermal fibroblasts from controls and DCMA patients with mild and severe cardiac dysfunction were provided 5.5 mM ^{12}C glucose in DMEM. These data are the average of three biological replicates per condition, with three separate technical replicates. Bars represent ± SEM of nine replicates, and ** represents $p < 0.005$ using Student's two-tailed t-test.
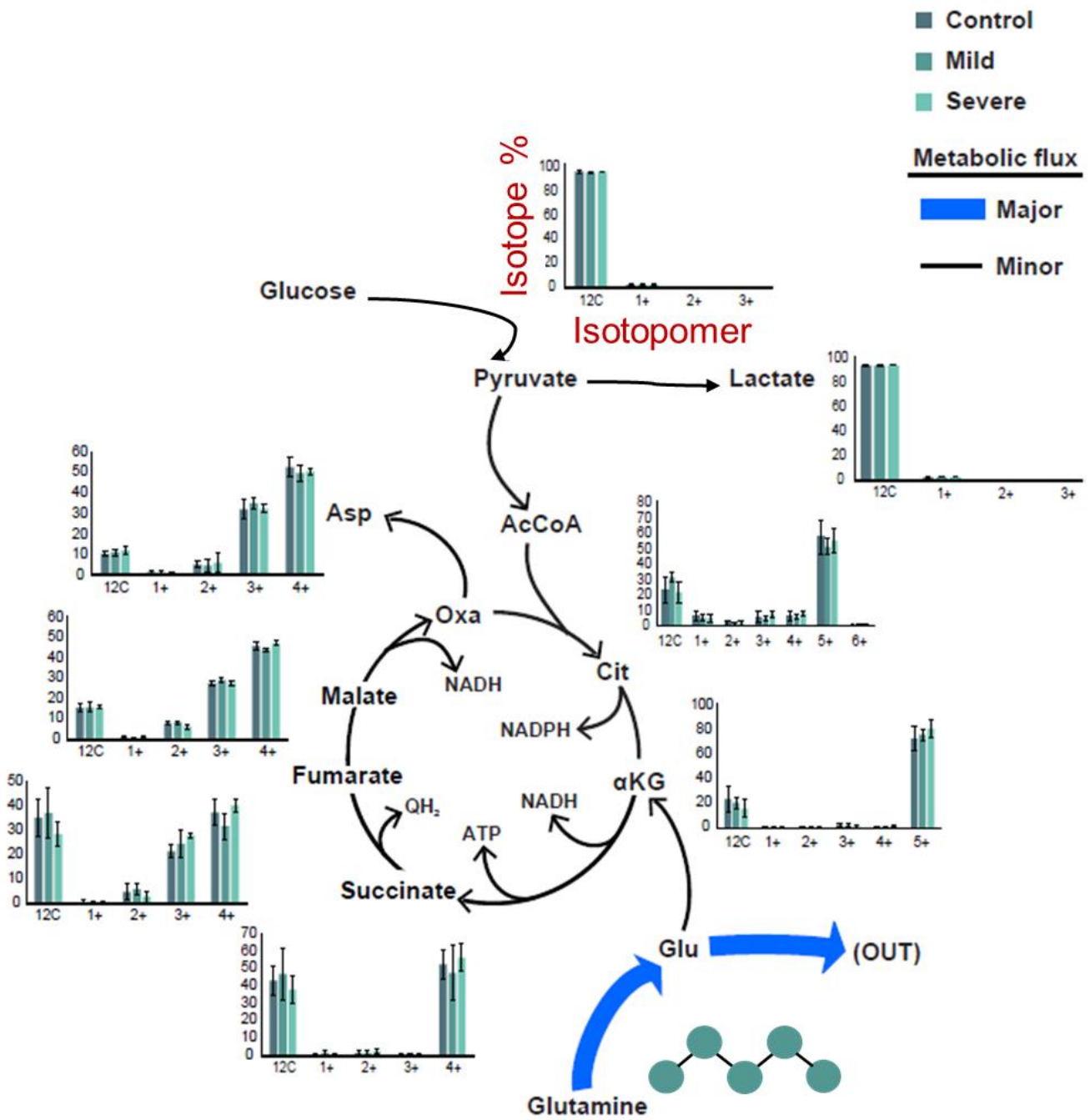
Figure 3.10 Intracellular steady state isotope enrichment of TCA cycle metabolites.

Dermal fibroblasts from controls and DCMA patients with mild and severe cardiac dysfunction were provided 5-^{13}C labelled glutamine in DMEM for 72 hours, then 24 hours incubation. Intracellular metabolites were extracted and isotope enrichment percentages were calculated from the signal intensities of the isotopomers of each metabolite. Blue arrows represent major flux of glutaminase reaction and glutamate excretion in DCMA (determined in 3.4.5). The bar graphs y-axes are isotope enrichment percentages from the total isotopomer pool and the x-axes are isotopomers. These data are the average of three biological replicates per condition, with two separate technical replicates. Bars represent ±SEM of six replicates. AcCoA represents acetyl-CoA; Asp, aspartate; Cit, citrate; Glu, glutamate; NADPH, NADH phosphate; Oxa, oxaloacetate; QH$_2$, Quinone in ETC complex II.

3.4.6 The glutaminase reaction rate is increased in DCMA cells

The first reaction of glutamine catabolism is the mitochondrial matrix glutaminase reaction. To determine if the biomarkers identified in Chapter 3.4.2 are directly derived from this mitochondrial reaction, the glutaminase inhibitor CB-839 was applied to the fibroblast model system. CB-839 is insoluble in water and so there was 0.1% DMSO present in the fibroblast medium. The addition of 0.1% DMSO to cell medium as a vehicle control did not appear to have an effect on cellular metabolism based on unaltered glucose uptake and lactate production. The concentration for CB-839 that did not interfere with glucose uptake yet affected glutamine metabolism was 0.1 µM (Figure 3.11). Thus, this concentration was used to determine the effects of CB-839 treatment on one severe DCMA fibroblast cell line and two control cell lines.

Although glutamine uptake remained the same (Figure 3.12), CB-839 treatment applied to both control and DCMA fibroblasts decreased their glutamate production (Figure 3.13). This overall decrease in glutamine metabolic flux is indicative of an inability to undergo the first reaction of this pathway, the glutaminase reaction. Moreover, inhibiting the mitochondrial glutaminase reaction resulted in diminishing glutamine-derived labelled glutamate secretion by both control and DCMA cells, suggesting that the glutaminase reaction rate is increased in DCMA (as DCMA cells normally produce more glutamine-derived labelled glutamate). Although CB-839 treatment was only conducted in three cell lines in this assay, its measurable effects on glutamine metabolism suggests that the rate of this metabolic flux may be increased in DCMA.
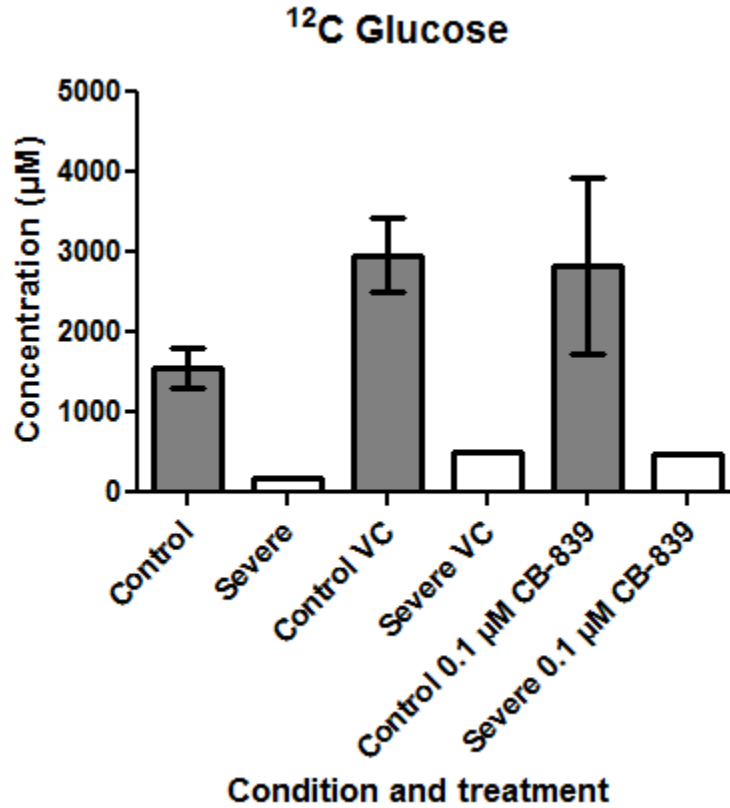
Figure 3.11 Normal glucose uptake is observed at 0.1 µM CB-839.

Glucose concentration (µM) in fibroblast medium after 48 hours incubation untreated, with 0.1%

DMSO vehicle control (VC), or with 0.1 µM glutaminase inhibitor CB-839. Two control fibroblast

cell lines and one severe DCMA fibroblast cell line were provided 5500 µM ^{12}C glucose in

DMEM. Bars represent ±SEM of two replicates.
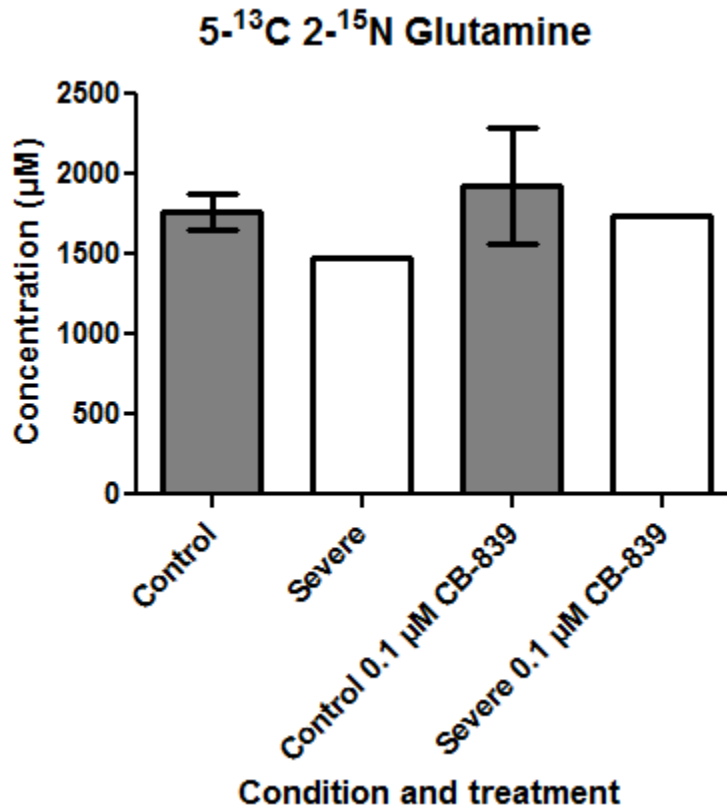
Figure 3.12 Dual stable isotope-labelled glutamine uptake from DMEM by fibroblasts treated with or without glutaminase inhibitor CB-839.

Glutamine concentration (µM) in fibroblast medium after 48 hours incubation. Two control fibroblast cell lines and one severe DCMA fibroblast cell line were provided 5-^{13}C 2-^{15}N stable isotope-labelled glutamine in DMEM. Control and severe were treated with 0.1% DMSO vehicle control, or with 0.1 µM CB-839. Bars represent ± SEM of two replicates.
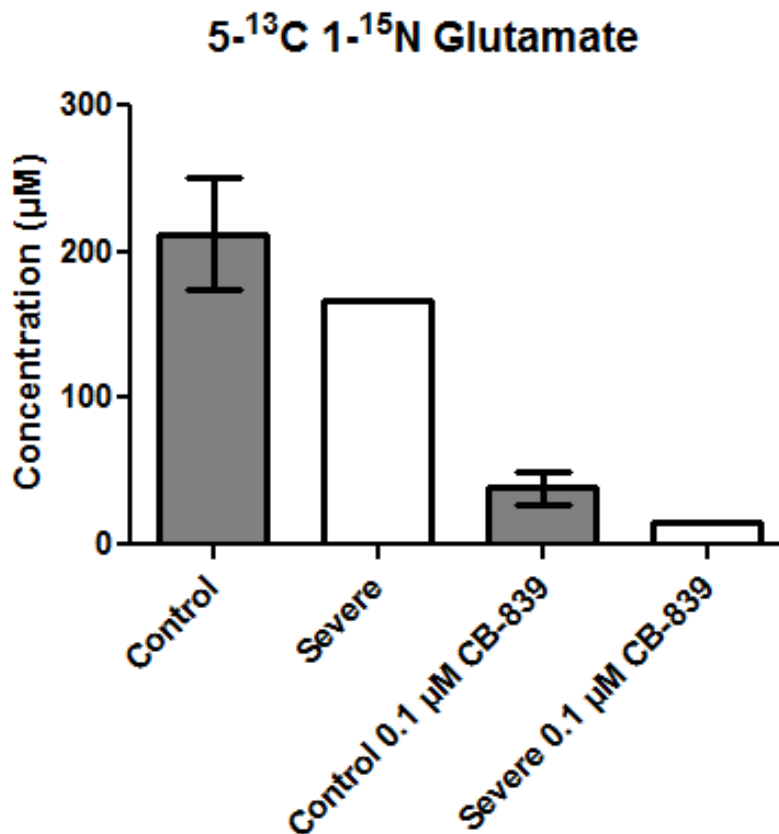
Figure 3.13 Glutamine-derived glutamate production by fibroblasts treated with or without glutaminase inhibitor CB-839.

$5\text{-}^{13}C$ $1\text{-}^{15}N$ labelled glutamate concentration (μM) in fibroblast medium after 48 hours incubation. Two control fibroblast cell lines and one severe DCMA fibroblast cell line were provided $5\text{-}^{13}C$ $2\text{-}^{15}N$ stable isotope-labelled glutamine in DMEM. Control and severe were treated with 0.1% DMSO vehicle control, or with 0.1 μM CB-839. Bars represent ± SEM of two replicates.

3.4.7 Blinded trial predictions

Using the biomarkers 5-^{13}C 1-^{15}N glutamine and 5-^{13}C glutamine, the clinical progression of nine DCMA cell lines of unknown disease severity (U1-U9) was predicted. Predictions of the blinded cohort were compared to the clinical data available for patients from which the cell lines were derived to determine if the predictions made were correct or incorrect. This allowed for the correct prediction of three severe cardiac dysfunction DCMA cell lines in a blinded cohort of nine DCMA cell lines (Figure 3.14): namely cell lines U1, U6, and U9. The other five blind DCMA cell lines (U2, U3, U4, U5, and U7) were correctly predicted to be either mild DCMA or control (unaffected), with the incorrect prediction of U8 as mild/control when in fact it was derived from a patient who is deceased. However, the details of the patient's death are not clear and it is not known if death was due to severe cardiac dysfunction and eventual heart failure. Overall, the positive predictive value (PPV) was 1.0 and the negative predictive value (NPV) was 0.83.
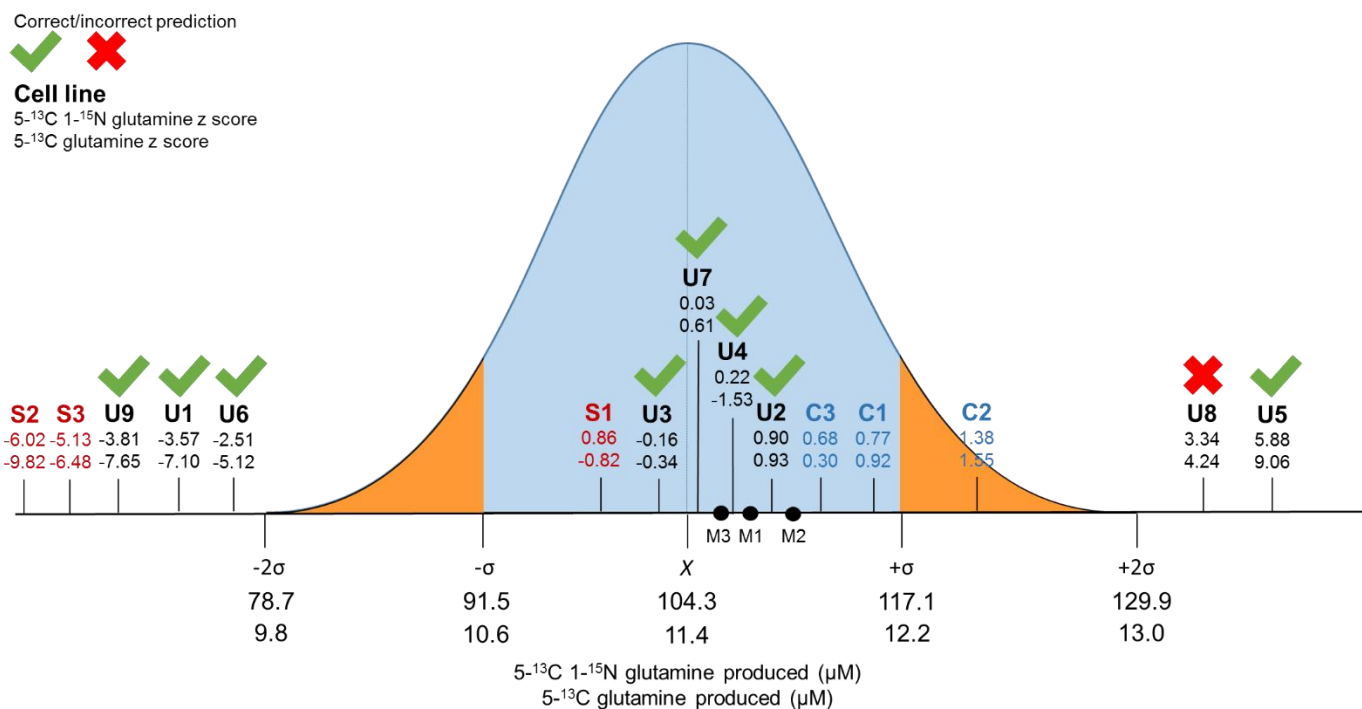
Figure 3.14 Blinded trial predictions of cell lines U1-9 based on biomarkers 5-^{13}C 1-^{15}N and 5-^{13}C glutamine.

The X-axis represents one or two standard deviations (σ or 2σ) above and below the average (X) concentrations of 5-^{13}C 1-^{15}N glutamine (top value) or 5-^{13}C glutamine (bottom value) produced by the mild DCMA population (cell lines M1, M2, and M3). M1-M3 are represented as dots and are shown for reference. Z scores of two different glutamine biomarkers are shown below unknown cell line names (U1-9) (as shown in legend in top left corner). Upon comparison to the clinical data available, predictions were deemed correct (green checkmark above) or incorrect (red X). Positive severe controls (S1, S2, and S3) are shown in red, and negative controls (C1, C2, and C3) are shown in blue.

3.5 Discussion

3.5.1 Altered glutamine metabolism: A previously undescribed DCMA metabolic phenotype

Due to its rarity, clinical heterogeneity, and lack of study, elucidating the disease mechanism of DCMA remains unclear. In discovering a previously unreported metabolic phenotype, this project has potentially provided a new direction for DCMA characterization and diagnosis. The expected phenotype of elevated 3-MGA and 3-MGC was not observed in this fibroblast model system. Although these acids are identified in the urine, cerebrospinal fluid and plasma of DCMA patients they may not be produced by dermal fibroblasts (Wortmann et al. 2012). However, in my fibroblast model, there was a metabolic phenotype we did not anticipate: increased glutamine consumption, increased glutamate and ammonium production, and decreased glutamine recycling. These data suggest altered glutamine metabolism in DCMA resulting in perturbed carbon and nitrogen fluxes.

Redox-stressed conditions due to deficiencies in mitochondrial energy production require carbon metabolites (such as in the LDH or GDH reactions) as an electron dump to regenerate NAD^+. In this case, the cells would exhibit increased lactate production compared to controls but this did not occur in DCMA cells. This was the first piece of evidence suggesting that ETC function in DCMA cells may be normal. Glutamate production is another potential electron dumping mechanism through the reverse GDH reaction, in which NADH donates electrons to an α-KG molecule along with an ammonium to produce glutamate. Increased glutamate production in DCMA was observed, however this also occurs through non-redox transamination reactions ALT and AST. Thus, increased glutamate production may not be indicative of electron dumping because of perturbed ETC function.

The primary pieces of evidence suggesting DCMA ETC function is normal was the absence of an increase in electron dumping metabolic flux, and the lack of differences in the intracellular isotope enrichment percentage profiles of DCMA fibroblasts compared to controls.

83

As discussed in Chapter 1.3, ETC deficient cells are expected to have altered 5-^{13}C glutamine-derived TCA cycle metabolite isotope labelling. This phenotype was not observed in DCMA, indicating that DCMA fibroblasts do not rely on electron dumping reactions for non-ETC associated ATP production.

We originally hypothesized that DCMA cells have inefficient ETC and mitochondrial ATP production, however, there was no evidence of electron dumping mechanisms observed in DCMA cells, as well as the intracellular usage of glutamine-derived carbon was normal in DCMA cells. Rather, DCMA cells exhibit altered glutamine metabolism. The mitochondrial fragmentation previously observed in DCMA cells may be a result of an ATP deficiency from glutamate insufficiently anaplerotically feeding into the TCA cycle as α-KG. The α-KG source in fibroblasts is primarily derived from glutamine, specifically around 70% of intracellular α-KG (Figure 3.10). This is a surprising finding as the primary biological role of fibroblasts is collagen production. It has been found that glutamate derived from glutamine, instead of being directed towards α-KG production and TCA cycle anaplerosis, is used for glycine and proline production for use in collagen synthesis (Hamanaka et al. 2019).

Limited glutamate stores within DCMA mitochondria limit α-KG stores, causing DCMA cells to be ATP deficient, which could lead to the previously observed fragmented DCMA mitochondria (Machiraju et al. 2019). Just as α-KG undergoes a reverse reaction to re-produce glutamate, these glutamate molecules can be re-aminated again to produce (or recycle) glutamine. The 5-^{13}C 1-^{15}N and 5-^{13}C glutamate produced in cells can undergo the glutamine synthetase reaction in which glutamate is aminated using ammonium and an ATP to produce glutamine, which is referred to as glutamine recycling. This produces 5-^{13}C 1-^{15}N and 5-^{13}C labelled glutamine, which were normally produced by control fibroblasts. Glutamine recycling normally occurs in peripheral tissues to deliver toxic ammonia to the liver, where it is converted to urea via the urea cycle (Ballester et al. 2019). It also occurs in hepatic cells to transfer

ammonia and/or provide glutamine for other hepatic cells (Nissim et al. 1999). This glutamine synthesis requires ATP and thus ATP-limiting conditions in DCMA cells exhibit decreased glutamine synthetase flux, or glutamine recycling.

Downstream of 5-^{13}C glutamine is 5-^{13}C glutamate and 5-^{13}C α-KG. 5-^{13}C α-KG can enter the oxidative TCA cycle to produce 4-^{13}C succinate and downstream 4-^{13}C metabolites. Alternatively, 5-^{13}C α-KG can be reductively carboxylated in the cytosol to produce 5-^{13}C (+5) citrate. This reductive flux of glutamine-derived α-KG is also normal in DCMA fibroblasts. This is indicated by the same isotope enrichment percentage for the intracellular +5 citrate isotopomer. This occurs via the cytosolic isocitrate dehydrogenase isoform in which an NADH molecule reduces and carboxylates 5-^{13}C α-KG using a ^{12}C HCO$_3^-$ to produce 5-^{13}C citrate. Normally this reductive carboxylation occurs for fat synthesis in cells, but can provide an electron dump for ETC-deficient cells, as shown in a previous study of cells with defective ETC complexes (Mullen et al. 2012). However, flux through this pathway was found to be normal in DCMA cells, which do not require electron dumping mechanisms because their ETC function is normal.

While flux through glutamine metabolic pathways is normal, the rate it occurs at is increased in DCMA. This is indicated by the increased glutamine consumption and glutamate production of DCMA fibroblasts. This should lead to an increase in intracellular nitrogen, as glutamine presents a major nitrogen source in addition to being a carbon source (Bhutia and Ganapathy 2016). Initially this implied that nitrogen metabolism might potentially play a role in the disease mechanism of DCMA. However, when ammonium production was measured it was found to also be increased in DCMA cells compared to control. The urea cycle normally occurs in hepatic cells, and other cell types normally excrete nitrogen in the form of glutamine through glutamine recycling (Ballester et al. 2019). There was no intracellular ^{15}N isotope labelling of ornithine or argininosuccinate (intermediates of the urea cycle), indicating that glutamine-derived nitrogen was not used for urea synthesis but rather was secreted out of the cell in the

85

form of ammonium. Mitochondrial ammonium diffuses out into the cytosol through an IMM aquaporin channel, and out of the cell through a plasma membrane aquaporin (Soria et al. 2010; Yang and Hinner 2015). The observed increased glutamine metabolic flux was not dedicated to nitrogen purposes, such as nucleotide or urea synthesis, but rather was excreted as ammonium (Lane and Fan 2015). This means DCMA cells are not utilizing the extra nitrogen derived from glutamine, but rather it is being excreted.

The identity of the reaction in DCMA responsible for the observed metabolic phenotypes may be glutaminase, as indicated by treatment with the glutaminase inhibitor CB-839. Upon CB-839 treatment, glutamine consumption was not affected. However, there was a decrease in 5-^{13}C 1-^{15}N glutamate production in both control and DCMA cells. Labelled glutamate production is downstream of glutaminase, indicating that this reaction rate is increased in DCMA cells, which have higher rates of labelled glutamate production. Limitations to the inhibitor assay that must be considered are that it was conducted in only two control and one DCMA cell lines and statistical analysis could not be conducted, and thus concrete conclusions regarding its effects on DCMA mitochondrial metabolism cannot be made until the assay is repeated using all DCMA cell lines. However, these data are promising in that there was a decrease in the normally increased DCMA metabolic phenotype upon inhibition of the glutaminase reaction.

The DCMA metabolic phenotype consists of increased glutamine uptake, increased glutamate and ammonium production, and decreased glutamine recycling. Increased glutamate and ammonium production may also be indicative of decreased cellular utilization of these molecules. Taken together, these data indicate altered glutamine metabolism in DCMA. Differences in concentrations of biomarkers were also normalized by looking at extracellular ^{13}C carbon flux, in which DCMA fibroblasts dedicated less glutamine-derived carbon to glutamine recycling, and dedicated slightly more to glutamate production. This metabolic phenotype is associated with the mitochondrion, as glutaminase isoforms localize to the matrix side of the

IMM in mammalian cells (Olalla et al. 2002; Perera et al. 1991). A measurable effect resulting from specific inhibition of the mitochondrial matrix enzyme glutaminase suggested the increased flux of this reaction in DCMA. This alteration in glutamine metabolism may occur as a compensatory mechanism because of the mutation in *DNAJC19*. Identifying the reaction and pathway with increased flux in DCMA identified sheds light on the possibilities of the native function of DNAJC19 and its ties to mitochondrial glutamine metabolism.

Although significant perturbations in glutamine metabolism were identified in DCMA using this model system, it is important to note that it was conducted using a fibroblast-based model. Fibroblasts do not play an obvious role in disease progression; thus, conclusions drawn from fibroblast metabolism may not fully or accurately depict the underlying disease mechanism. However, this study presents the first robust study of *in vitro* DCMA metabolism which has produced a hypothesis that can be investigated with future studies.

3.5.2 Applications in clinical diagnostics to predict DCMA patient disease prognosis

DCMA is initially diagnosed through identifying increased levels of the organic acids 3-MGA and 3-MGC, and confirmed by molecular-based DNA sequencing. While diagnostic, the levels of these acids in patients are not representative of disease, specifically cardiac dysfunction, severity. Thus, elevated 3-MGA and 3-MGC are not useful in predicting disease progression in DCMA patients. Current diagnostics of DCMA do not inform physicians of the degree of cardiac dysfunction, causing delays in implementing effective treatments such as timely heart transplants, leading to mortality in DCMA patients.

The robust DCMA metabolic phenotype I have observed not only associates with DCMA, but also tracks with clinical progression of patients. Thus, the fibroblast model system presents a potential clinical diagnostic tool. Fibroblasts derived from DCMA patients who suffered from higher degrees of heart failure due to dilated cardiomyopathy exhibited a more dramatic

glutamine recycling phenotype. The blinded trial successfully predicted the severe cell lines correctly by comparing predictions with the clinical data for the blinded cell lines. U1 and U6 fibroblast cell lines were revealed to be derived from deceased DCMA patients who suffered from heart failure, and U9 is derived from a DCMA patient with mildly reduced LV function on medical therapy including digoxin. One outlier was U8, predicted to not be severe, died of heart failure and may have had severe cardiac dysfunction; however, due to limited data, the details of the patient's cardiac dysfunction death are not clear. Another drawback of the blinded assay is the positive severe DCMA control, cell line S1, aligned within the mild population. However, the promising high PPV and NPV values introduce this assay as a potential diagnostic tool to predict severe cardiac dysfunction and heart failure in DCMA patients. This is crucial to plan for the most effective treatments, such as drug intervention, entering heart transplantation lists early on, or receiving mechanical circulatory support.

The glutamine recycling biomarkers present a useful precision diagnostics tool, which successfully predicted disease severity in eight blinded DCMA fibroblast cell lines through a blinded trial. Skin biopsies are a relatively easy and standardized procedure in a medical setting; thus, fibroblasts are a feasible tool to predict disease severity in DCMA patients.

3.5.3 Proposed novel model for DNAJC19 function

Knowledge of the underlying disease mechanism of DCMA is limited because of the unknown function of the DNAJC19 protein. This study may have uncovered the metabolic consequences of mutations in the *DNAJC19* gene and potentially the underlying disease mechanism. This will allow for a better understanding of the disease and more targeted therapeutic treatments. Currently, it is believed that DCMA arises from perturbed mitochondrial function due to deficiencies in mitochondrial protein import or structure. However, this is based on ambiguous, unconfirmed arguments, such as the BLAST sequence protein homology or the

88

apparent protein-protein interaction between DNAJC19 and PHB2 (Davey et al. 2006; Richter-Dennerlein et al. 2014). These studies suggest the native function of DNAJC19, but do not specifically address the direct metabolic consequences of a mutation in the gene.

My recent analysis of DCMA cellular metabolism identified normal TCA cycle metabolic flux and significant differences in glutamine metabolism. Current models of DCMA do not explain the strong metabolic phenotype identified, thus here we present a new potential model for DCMA and the native function of DNAJC19. Altered glutamine metabolic flux in DCMA fibroblasts implies the native function of DNAJC19 may lie in mitochondrial glutamine metabolism. A missing piece of this puzzle was the identification of the DNAJC19 interactome, a large-scale analysis conducted by Huttlin et al., in which all protein-protein interactions of every protein within HEK293T cells were robustly identified. This was done through affinity purification of tagged proteins followed by MS: 13,000 tagged open reading frames (ORFs) were constructed, baits and preys were immuno-purified, and interacting partners were identified using MS. Protein-protein interactions allow for the assembly of proteins into complex networks to carry out their specific cellular functions (Huttlin et al. 2017).

DNAJC19 interacts with several proteins, some well characterized and some with unknown function (Table 3.1 and Figure 3.15). The interaction partner of DNAJC19 that best explains the observed metabolic phenotype in fibroblasts and potentially play a role in DCMA is SLC1A1, a glutamate transporter that imports glutamate across the plasma and endosome membranes. SLC1A1 transports glutamate across neuronal plasma membranes in a sodium-dependent manner (Huttlin et al. 2017; Schweppe et al. 2018; Zerangue and Kavanaugh). However, its subcellular location has not been characterized in all cell types, and its potential interaction with DNAJC19 (an IMM protein) implies it may function as a mitochondrial glutamate importer in fibroblasts (Davey et al. 2006). If the function of this transporter relies on DNAJC19 and this transporter was one of the primary mechanisms of mitochondrial glutamine import, then

DCMA cells may be unable to properly import glutamate into the mitochondria. This would

produce the observed metabolic phenotypes of increased glutamine uptake, glutamate

production, ammonium production, and decreased glutamine recycling.

Table 3.1 DNAJC19 interacting proteins proposed by Huttlin et al. and their known or proposed functions. Interacting partners are ordered from highest to lowest probability. Information adapted from Huttlin et al. and NCBI (Huttlin et al. 2017; NCBI).

Protein	Proposed cellular function
AFG3L2 (AFG3 like matrix AAA peptidase subunit 2)	Mitochondrial ATP-dependent protease, helps in maturation of paraplegin, a mitochondrial metalloprotease with roles in motility, organelle biogenesis, protein folding, and proteolysis
SPACA1 (Sperm acrosome associated 1)	Known for its association to the sperm acrosome membrane and relates to sperm/egg fusion
ATP2A1 (ATPase Sarcoplasmic/Endoplasmic Reticulum Ca2+ (SERCA2))	ATPase Sarcoplasmic/Endoplasmic Reticulum Ca2+ (SERCA) Transporting pump in Sarcoplasmic/ER reticula. Uses ATP to pump calcium from cytosol to sarc/ER lumen, involved in muscle cell contraction.
MAGEA8 (Melanoma Antigen Gene family member A8)	Proposed to play a role in embryo development and tumour progression
PAM16 (Presequence translocase associated motor 16)	Iinvolved in cytokine signaling and ATP-depedent protein translocation of nuclear-encoded proteins into the mitochondrial matrix. May be important in reactive oxygen species (ROS) homeostasis
CD53	Cell growth regulation and motility
RAMP2 (Receptor activity modifying protein 2) (RAMPs are have single transmembrane domains with an extracellular N terminus and a cytoplasmic C terminus)	Membrane protein that regulates calcium transport by transporting calcitonin-receptor-like receptors (CRLR) to the plasma membrane
TSPAN5 (Transmembrane 4 superfamily protein, tetraspanin 5)	Transmembrane 4 superfamily protein (tetraspanin). Responsible for cell transduction events to regulate cell development.

SLC5A6 (Solute carrier family 5 member 6)	Transports pantothenate (vitamin B5), biotin and lipoate in the presence of sodium.
SLC1A1 **(Solute carrier family 1 member 1)**	**High-affinity glutamate transporter, also transports aspartate**
AQP3 (Aquaporin 3)	In basal lateral membrane of kidney collecting ducts, and present in skin for skin hydration
RANBP6 (RAs-related Nuclear binding protein 6)	Protein import into the nucleus as a nuclear transport receptor
PTH2R (Parathyroid hormone 2 receptor)	Receptor for parathyroid hormone, GPCR family 2
SLC22A4 (Solute carrier family 22 member 4)	Related to cation (sodium) transport, transport by this protein is ATP dependent
ACVR2B (Activin A receptor type 2B)	Activin type 2 receptor, growth factor receptor
P2RX4 (Purinergic receptor)	Purinoreceptor for ATP, ligand-gated ion channel, calcium permeable (P2X4 receptors have been implicated in the regulation of cardiac function, ATP-mediated cell death, synaptic strengthening, and activating of the inflammasome in response to injury)
CORO7 (Coronin 7)	Regulates anterograde Golgi to endosome transport and maintains Golgi apparatus morphology
HCRTR2 (Hypocretin receptor 2)	GPCR involved in the regulation of feeding behavior. Triggers more cytoplasmic calcium when neuropeptide orexin-A binds
FPR1 (Formyl peptide receptor 1)	Formyl peptide receptor 1, G protein coupled receptor (GPCR) with role in phagocytic cells for host defense and inflammation
GHRL (Ghrelin and obestatin prepropeptide)	"Hunger hormone" which signals to the body that regulates appetite
UGT1A5	Enzyme in glucuridination pathway (transforms small lipophilic molecules like

|	
(UDP-glucuronosyltransferase)	steroids, hormones, drugs into water-soluble, excreted metabolites
SLC37A3 (Solute carrier family 37 member 3)	Glucose-6-P or glycerol-3-P transmembrane transporter
SLC15A1 (Solute carrier family 15 member 1)	Protein uptake in small intestine epithelium
DUOXA2 (Dual oxidase maturation factor 2)	Required for the maturation and the transport from the endoplasmic reticulum to the plasma membrane of functional dual oxidase 2, an NADPH oxidase. May play a role in thyroid hormone synthesis.
SLC2A12 (Solute carrier family 2 member 12)	Glucose transporter, GLUT12, homology to insulin-receptive GLUT4
TSPAN15 (Tetraspanin 15)	Mediates signal transduction events that play a role in the regulation of cell development, activation, growth and motility. Regulates maturation and trafficking of metalloprotease ADAM10
ABTB2 (Ankyrin repeat and BTB domain containing 2)	May be involved in the initiation of hepatocyte growth.
STK36 (Serine/Threonine kinase 36)	Analogous to drosphila protein in Hedgehog signaling (for cell differentiation)
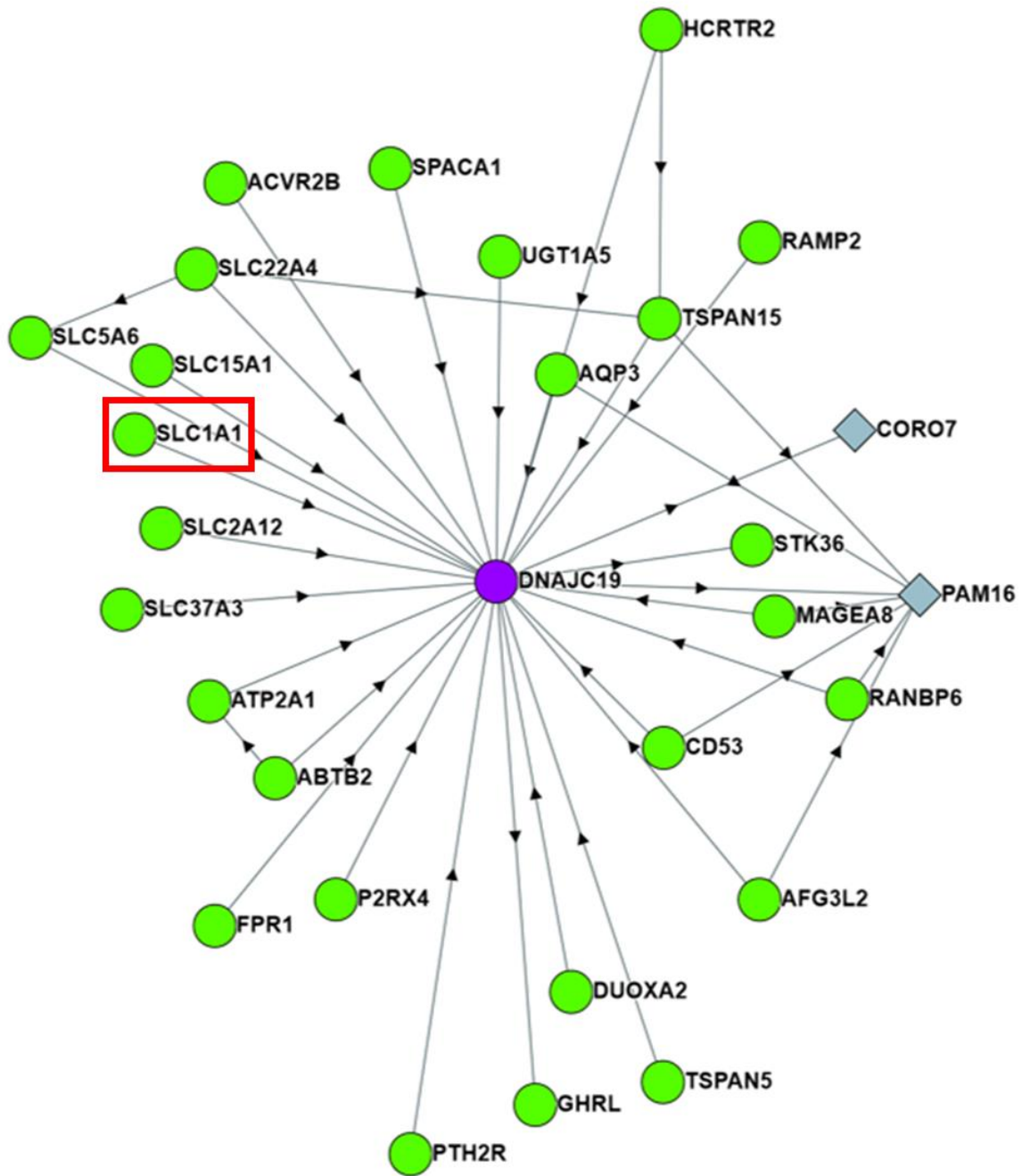
Figure 3.15 DNAJC19 interactome.

Protein-protein interactions of the DNAJC19 protein determined by Huttlin et al. SLC1A1 is

highlighted with a red box. Figure adapted from BioPlex Display by Huttlin et al (Schweppe et al.

2018).

Perturbations in glutamine metabolic flux indicates a mitochondrial phenotype as glutamine metabolism occurs within the mitochondrial matrix. As indicated by the glutaminase inhibitor data, DCMA cells may exhibit increased rate of the mitochondrial matrix glutaminase reaction, which converts glutamine to glutamate and ammonium by hydrolysis. If DCMA cells are not utilizing this reaction for nitrogen purposes (as the fibroblasts excrete nitrogen out in the form of ammonium), and have perturbed mitochondrial glutamate import due to impaired ability to import glutamate into the mitochondria, then this may potentially be a compensatory mechanism for an inability to import cytosolic glutamate into the mitochondrial matrix. This normally occurs through glutamate proton symporters, but SLC1A1 may present as one of the primary functioning glutamate importers in fibroblasts (Goubert et al. 2017; Fiermonte et al. 2002). DCMA cells import cytosolic glutamine instead of glutamate, and deaminating glutamine to glutamate within the matrix. This flux replenishes mitochondrial matrix glutamate stores for use in the TCA cycle. Another result of this is increased ^{15}N ammonium production. This would manifest as the metabolic phenotypes of increased glutamine consumption, and increased glutamate and ammonium production. Increased glutamine uptake into the mitochondria compensates for an inability of DCMA mitochondria to import glutamate. Increased 5-^{13}C 1-^{15}N glutamate production within the mitochondrial matrix from the increased glutaminase reaction flux would result in glutamate moving down its gradient across the IMM and plasma membrane, secreted out of the cell. The glutamate produced can also be further metabolized to produce 5-^{13}C α-KG. This metabolite can undergo a reverse reaction to re-produce glutamate, which is excreted out of the cell. This occurs by the AST transamination reaction where 5-^{13}C α-KG receives an unlabelled nitrogen from aspartate to produce 5-^{13}C glutamate and oxaloacetate. Both 5-^{13}C 1-15N and 5-^{13}C glutamate production were increased in DCMA, indicating increased glutaminase reaction flux. These metabolic mechanisms are described in Figure 3.16.
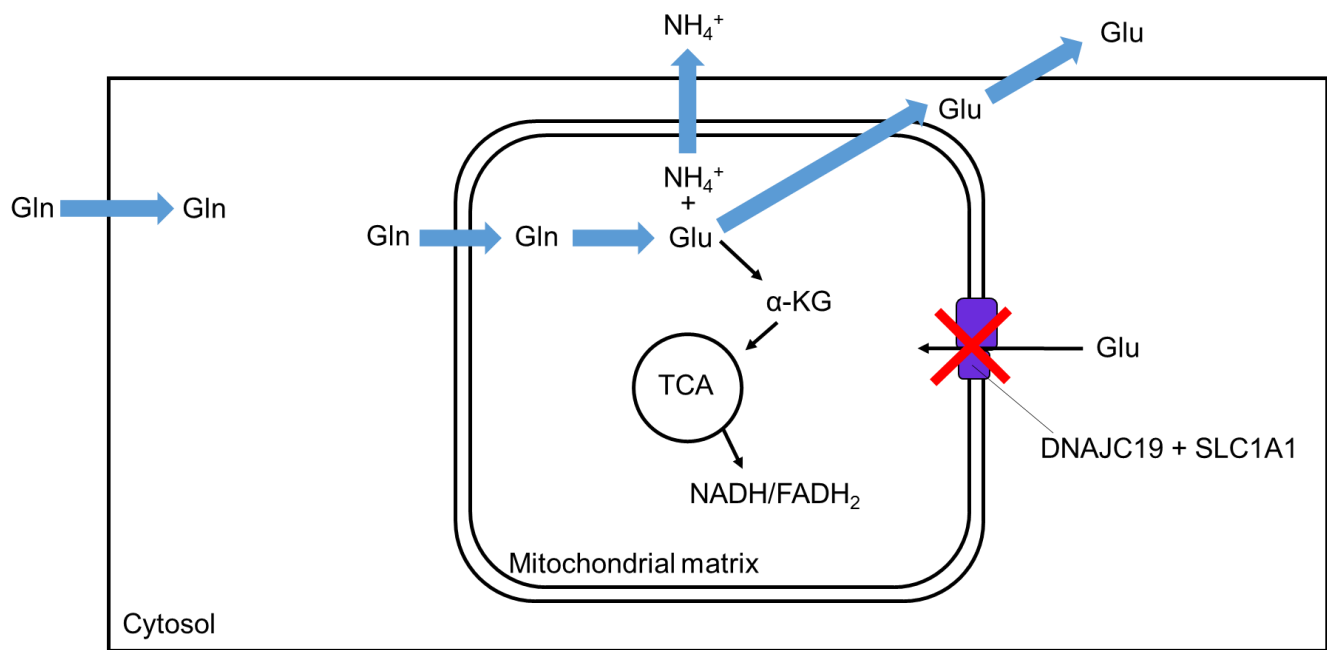
Figure 3.26 A Putative Model for DCMA compensatory glutamine metabolism.

DCMA cells with a nonfunctional DNAJC19 have an inability to import cytosolic glutamate into the mitochondrial matrix (indicated by a red X). A possible compensatory mechanism to replenish mitochondrial glutamate stores is to import glutamine instead, which undergoes the mitochondrial matrix glutaminase reaction to produce glutamate (which undergoes further mitochondrial metabolic reactions, or is exported out) and ammonium (which is exported out). Larger blue arrows represent metabolic fluxes increased in DCMA as compensatory mechanisms. Black boxes represent membranes. Gln represents glutamine; Glu glutamate; NH_4^+ ammonium.

It has been previously reported that DCMA cells exhibit fragmented mitochondria, as well as increased ROS (Machiraju et al. 2019). Mitochondrial structure and function are linked through the ETC requiring optimal mitochondrial structure, and alterations in either was expected to cause altered carbon usage with increased flux in electron dumping pathways. However, as discussed previously, there are no ETC deficiencies in DCMA; this is indicated by the absence of electron dumping mechanisms or altered carbon isotope enrichment profiles of TCA cycle metabolites. Glutamate is a key central carbon metabolite involved in mitochondrial metabolism and relies on proper import from the cytosol (Amoedo et al. 2016). An inability to import glutamate may introduce energy production deficiencies, causing the observed cardiac phenotype in DCMA patients. Thus, the root cause of this is not perturbations in mitochondrial energy production, but rather this is an effect of the new proposed disease mechanism, being altered mitochondrial glutamine metabolism. The potential interaction between DNAJC19 and SLC1A1 may be required for proper mitochondrial glutamate import to anaplerotically feed the TCA cycle, a central carbon metabolic pathway. A mutation in DNAJC19 may disturb this function and therefore interrupt glutamine metabolism and efficient ATP production by the ETC, leading to the observed mitochondrial structure deficiencies in DCMA. However, this hypothesis is less supported by the metabolic data collected, which indicates normal TCA cycle metabolism in DCMA fibroblasts.

Previous studies of DCMA have suggested the underlying disease mechanism to be attributed to perturbations in mitochondrial function (through an inability to import nuclear encoded proteins, which include ETC complex subunits), or structural deficiencies (through an inability to normally undergo cardiolipin remodeling) (Davey et al. 2006; Richter-Dennerlein et al. 2014). The DCMA metabolic phenotype characterized suggests that DCMA may arise from a mitochondrial transporter and glutamine metabolism problem, which hints to the native function of DNAJC19. My model system, along with the proposed protein-protein interaction with a

glutamate transporter identified by Huttlin et al., provides a new possible mechanism for DCMA and DNAJC19's involvement with mitochondrial glutamate import (Huttlin et al. 2017). Disabling the DNAJC19 and SLC1A1 protein-protein interaction may result in a deficiency in mitochondrial glutamate stores. This is compensated for by increased glutamine uptake and the mitochondrial matrix glutaminase reaction flux to replenish mitochondrial glutamate stores. However, this interaction must be confirmed experimentally.

Although this proposed new model of DNAJC19 function may explain the observed metabolic phenotype, there are existing limitations. Firstly, fibroblasts do not play an obvious role in disease progression so whether glutamate import is tied directly to the underlying disease mechanism of DCMA is not clear, and metabolic studies of other DCMA cell types must be conducted to confirm this. Also, it may be that altered mitochondrial glutamate import is not the primary underlying disease mechanism of DCMA, but rather is a contributor to disease progression, among a variety of other mechanisms. Finally, mutations in the *SLC1A1* gene causes dicarboxylic aminoaciduria, a neurological disorder with very different clinical presentation to DCMA (Bailey et al. 2011). This calls the proposed function of DNAJC19 and SLC1A1 in mitochondrial glutamate import into question. However, this model presents the best fit using current knowledge of the DNAJC19 protein, the DNAJC19 interactome, and the robust DCMA metabolic phenotype identified.

3.6 Conclusions

Using the analytical methods developed in Chapter 2, a novel glutamine metabolism phenotype was identified in DCMA. This previously undescribed metabolic phenotype suggests a possible novel underlying disease mechanism for DCMA. Previous studies attributed the clinical presentations of DCMA to be due to perturbed mitochondrial function. My data suggests that while mitochondrial function in the context of the TCA cycle appears normal, DCMA exhibits

measurable perturbations in glutamine metabolic flux. This novel finding in DCMA metabolism potentially adds new insight to this disease as a disorder affecting glutamine metabolism, specifically through deficiencies in mitochondrial glutamate import, rather than perturbed mitochondrial function. This is suggested through the potential protein interactions of DNAJC19 and a glutamate transporter, and how it relates to the observed metabolic phenotype. Moreover, the metabolic phenotype appears to distinguish between disease severities; thus, the fibroblast model system has potential applications as a clinical diagnostic tool to predict DCMA patient disease prognosis, allowing the implementation of timely treatments and improve patient's quality of life.

Chapter Four: CONCLUDING REMARKS

My M. Sc. work presents novel insight into the underlying metabolic underpinnings of DCMA, an under-characterized and severe disorder. I developed a fibroblast-based model system, which was used to characterize DCMA; from this, I identified a novel metabolic phenotype in six patient fibroblast cell lines that may describe the underlying disease mechanism. I propose a new model of DCMA, with the native function of DNAJC19 potentially lying in mitochondrial glutamate transport. Specifically, the DCMA mutations resulting in a nonfunctional DNAJC19 causes perturbed glutamine metabolic flux to replenish mitochondrial glutamate stores. The glutamine recycling metabolic phenotype was also found to map to severity; thus, it was utilized as a precision diagnostic tool to successfully predict the clinical progression of eight DCMA patient-derived cell lines.

Limitations to this study was that it only examined one cell type that is not obviously involved in disease progression. Application of the metabolic flux assays to other cell types such as DCMA patient-derived cardiomyocytes will yield more conclusive results of the underlying disease mechanism which causes heart failure in patients. To confirm the potential DNAJC19 function, protein-protein interaction studies must be conducted to confirm the DNAJC19/SLC1A1 interaction *in vitro*. In addition to this, the glutaminase inhibitor assay must be conducted with the appropriate cell line replicates to confirm the findings of Chapter 3.4.6. Lastly, an important study that must be conducted is the generation of *DNAJC19* knockout cell lines using small interfering ribonucleic acid (siRNA) and applying them to the developed assays to confirm that the observed DCMA metabolic phenotype is related to the genetic basis of disease.

Applications of these data generated from my thesis paves the way to better understand DCMA potentially as a disorder of mitochondrial amino acid metabolism, and predict DCMA patient disease progression to better implement effective and timely treatments.

In addition to characterizing the underlying disease mechanism of DCMA and predicting disease progression in patient-derived cell lines using metabolomics, the biochemical assay developed was used to determine the effects of various metabolism-targeting drugs on DCMA fibroblasts. Mitochondrial structural studies were also conducted to examine the effects of inhibiting mitochondrial function on structure.

Drug therapeutic efficacy in DCMA

Current treatments of DCMA are based on adult acquired heart disease and have minimal efficacy. One promising treatment for DCMA is digoxin, a medication used to treat heart failure (Greenway et al. 2018). The proposed metabolic mechanism of action of this drug is via the inhibition of the sodium-potassium ATPase, causing an increase in intracellular and mitochondrial matrix calcium concentrations. Calcium is a known activator of TCA cycle dehydrogenase enzymes, so it would be expected that digoxin treatment stimulates TCA cycle flux (Finkel et al. 2015). Moreover, intracellular calcium activates mitochondrial glutamate import via the glutamate/aspartate antiporter located in the IMM; this function is required for shuttling cytosolic electrons into the mitochondrion for use in the ETC (Sakurai et al. 2010). Thus, an increase in glutamine metabolic flux observed in DCMA cells treated with digoxin is expected.

Another potential therapeutic is the novel peptide Szeto-Schiller peptide (SS-31) (D-Arg-2′6′-dimethylTyr-Lys-Phe-NH2), which is proposed to protect cardiolipin species from oxidation by mitochondrial ROS (Machiraju et al. 2019; Szeto 2014). ROS are produced as a result of mitochondrial dysfunction, so treatment of DCMA cells with SS-31 would be expected to be effective in improving mitochondrial structure and improving function if the disease mechanism lies in cardiolipin remodeling (Machiraju et al. 2019). China Peptides synthesized an SS-31 derivative compound which lacks the methylated tyrosine residue (D-Arg-Tyr-Lys-Phe-

NH2), named 366401. 366401 was expected to not induce the same effects as SS-31 due to its lacking of the structural component proposed to be responsible for its anti-oxidant effects (Escribano-Lopez et al. 2018).

The rarity and heterogeneity of DCMA prevents the evaluation of potential therapeutics through large, randomized clinical trials, so the use of *in vitro* modeling with patient-derived cells presents the best option to identify effective therapeutics (Rohani et al. 2017). The developed biochemical assay was used to evaluate potential novel drug therapeutics that target mitochondria by determining the effects on the DCMA metabolic phenotype.

The fibroblast model system tested the efficacy of the metabolism-targeting therapeutics SS-31, 366401, and digoxin. Normal glucose uptake by fibroblasts indicates viable cells with normal metabolism, which was used to determine effective concentrations of each drug. SS-31 and 366401 were synthesized by China peptides (Wu et al. 2017). Effective concentrations for SS-31 treatment of DCMA fibroblasts were previously determined in which 24 hours incubation with 100 nM of SS-31 decreased mitochondrial fragmentation and ROS production in DCMA fibroblasts (Machiraju et al. 2019). The SS-31 derivative compound 366401 was expected to act in a similar mechanism and thus 100 nM was used. The effective concentration for digoxin was found to be 20 nM.

The effects on the metabolic phenotype were determined using the developed fibroblast assay (Figure A1). SS-31 and 366401 protect cardiolipin, a mitochondrial lipid vital for proper structure and function, from oxidation by ROS. Treatment with these drugs was found to have no effect on glutamate production by DCMA cells, indicating that mitochondrial cardiolipin metabolism does not play a role in the observed DCMA metabolic phenotype. This is also confirmed by DCMA lipidomics studies in which levels of cardiolipin species were measured and found to be normal in DCMA fibroblasts. In this same study, however, mitochondrial

fragmentation was improved upon SS-31 treatment, thus the connect between mitochondrial structure and function remains unclear (Machiraju et al. 2019).

Digoxin has proved to be an effective treatment for heart failure in DCMA patients (Greenway et al. 2018). Although its proposed mechanism is metabolic in nature by activating mitochondrial dehydrogenases to increase ATP production, digoxin did not decrease the observed DCMA metabolic phenotype of glutamate production, but rather increased it. I speculate that improvements in clinical outcome of DCMA patients upon treatment with digoxin occur most likely because of increased calcium availability for cardiac muscle, thereby improving cardiac function, and not due to improvements in mitochondrial energy production although this remains to be tested in cardiomyocytes.

Targeting mitochondrial structure or mitochondrial ATP production did not affect DCMA cells as the disease mechanism lies in glutamine metabolism. Specifically, targeting and upregulating glutamate import into the mitochondrial matrix may prove to be a more effective strategy to treating DCMA.
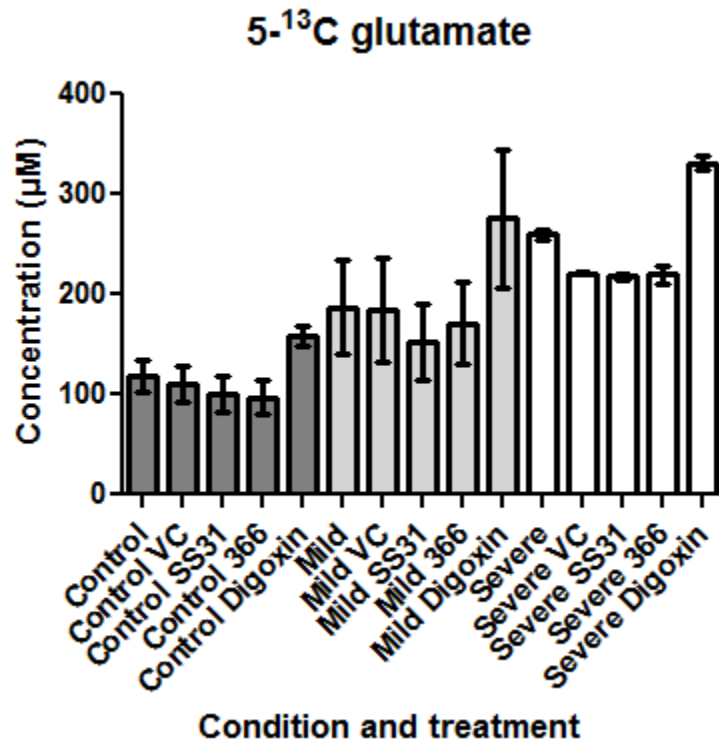
Figure A1 Effect of various drug therapeutics in fibroblasts.

Stable isotope-labelled glutamate concentration (µM) in fibroblast medium after 48 hours incubation. Dermal fibroblasts from controls and DCMA patients with mild and severe cardiac dysfunction were provided $5\text{-}^{13}C$ stable isotope-labelled glutamine in DMEM. VC represents 0.1% DMSO vehicle control, SS-31 represents 100 nM SS-31 treatment, 366 represents 100 nM 366401 treatment, and Digoxin represents 20 nM digoxin treatment. These data are the average of two biological replicates per condition, with three separate technical replicates. Bars represent ± SEM of six replicates.

Mitochondrial structure studies using immunocytochemistry

In addition to functional studies using metabolomics, I looked into the effects of induced mitochondrial inhibition on mitochondrial structure. This was to investigate the relationship between mitochondrial structure and function in which inhibition of ETC function would induce mitochondrial fragmentation due to the production of ROS and mitochondrial lipid oxidation.

The ETC complex III inhibitor Antimycin A (AMA) was applied to control fibroblasts using the developed fibroblast-based model system (Ma et al. 2011). Immunocytochemistry was conducted using mitochondrial membrane marker TOMM20 primary antibody stain. Fibroblasts were imaged using a Zeiss LSM880 high-resolution confocal microscope and 30 random individual fibroblasts were taken for mitochondrial fragmentation quantification. Mitochondrial fragmentation was calculated using mean network size in the ImageJ Fiji software package (Schindelin et al. 2012). AMA treatment increased mitochondrial fragmentation, resulting in a decreased mean network size (Figures A2 and A3). Less than 60 replicates were used in the mitochondrial fragmentation calculation because less than 30 fibroblasts could be found in the AMA treated cells.

Chemical inhibition of mitochondrial function in fibroblasts was found to affect mitochondrial structure, suggesting the two may be linked. However, the production of ROS is known to be derived from a variety of sources and not mitochondrial dysfunction alone, resulting in mitochondrial fragmentation due to lipid oxidation (Ježek et al. 2018). Thus, conclusions on the links between mitochondrial structure and function cannot be made from this study alone.
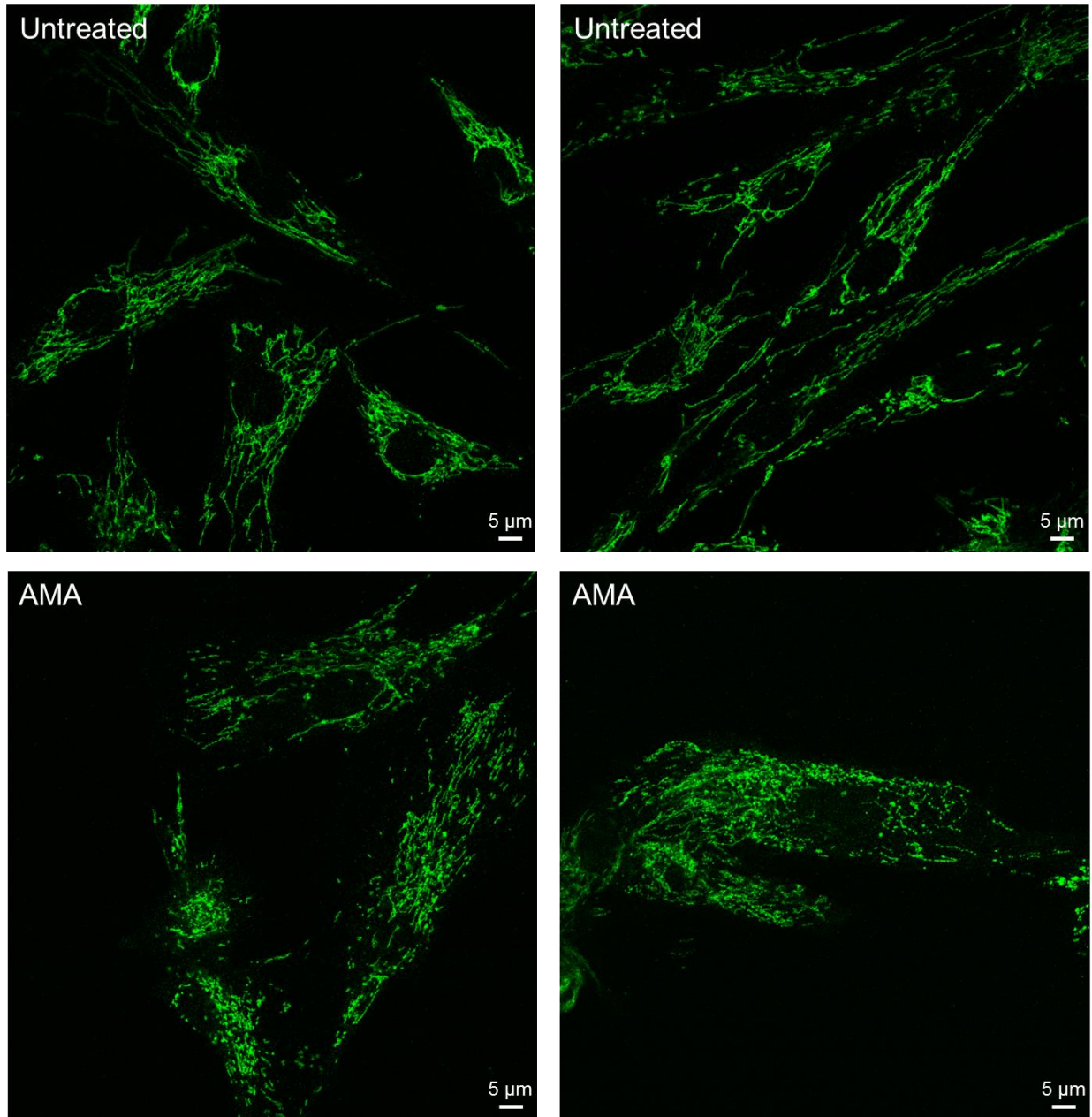
Figure A2 AMA treatment increased fragmentation of fibroblast mitochondria.

Control fibroblasts untreated (top panels) or treated (bottom panels) with 50 μM AMA were

stained with TOMM20 primary antibody. Scale bar measures 5 μm. Figures were obtained using

ImageJ Fiji package (Schindelin et al. 2012).
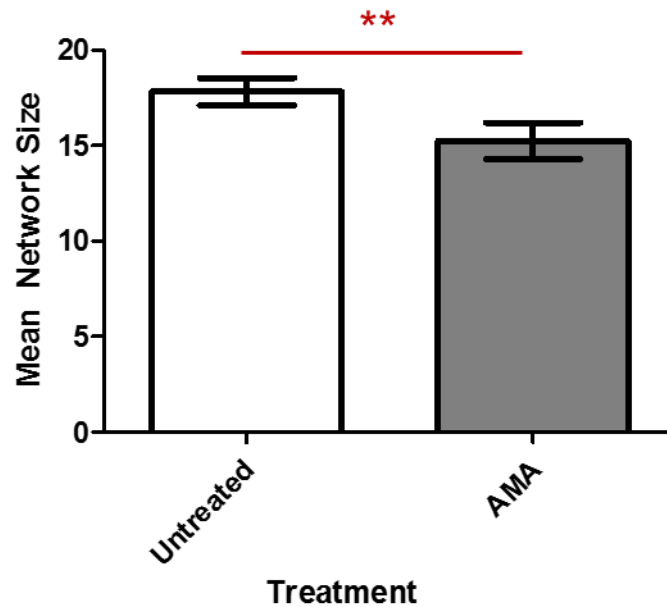
Figure A3 Mean network size of fibroblast mitochondria treated with AMA.

Fibroblasts were incubated in DMEM containing 50 µM Antimycin A for 24 hours. These data are the average of 30 random individual cells of each condition, which are derived from two biological replicates with one separate technical replicate. Bars represent ± SEM of 60 untreated replicates or 30 AMA replicates, and ** represents $p < 0.005$ using Student's two-tailed t-test.

References

1.   Davey, K. M. *et al.* Mutation of DNAJC19, a human homologue of yeast inner mitochondrial membrane co-chaperones, causes DCMA syndrome, a novel autosomal recessive Barth syndrome-like condition. *J. Med. Genet.* **43**, 385–93 (2006).

2.   Meyer-Rochow, V. B. & Gal, J. Pressures produced when penguins pooh - Calculations on avian defaecation. *Polar Biol.* **27**, 56–58 (2003).

3.   Cox, G. F. Diagnostic Approaches to Pediatric Cardiomyopathy of Metabolic Genetic Etiologies and Their Relation to Therapy. *Prog. Pediatr. Cardiol.* **24**, 15–25 (2007).

4.   Schmiedel, J., Jackson, S., Jochen, S. & Heinz, R. Mitochondrial Cytopathies. *J. Neurol.* **250**, 267–277 (2003).

5.   Diaz, F., Kotarsky, H., Fellman, V. & Moraes, C. T. Mitochondrial disorders caused by mutations in respiratory chain assembly factors. *Seminars in Fetal and Neonatal Medicine* **16**, 197–204 (2011).

6.   MacKenzie, J. A. & Payne, R. M. Mitochondrial protein import and human health and disease. *Biochim. Biophys. Acta* **1772**, 509–23 (2007).

7.   Ojala, T. *et al.* New mutation of mitochondrial DNAJC19 causing dilated and noncompaction cardiomyopathy, anemia, ataxia, and male genital anomalies. *Pediatr. Res.* **72**, 432–437 (2012).

8.   Ucar, S. K. *et al.* Previously Unreported Biallelic Mutation in DNAJC19: Are Sensorineural Hearing Loss and Basal Ganglia Lesions Additional Features of Dilated Cardiomyopathy and Ataxia (DCMA) Syndrome? in *JIMD reports* **35**, 39–45 (Wiley-Blackwell, 2016).

9.   Al Teneiji, A., Siriwardena, K., George, K., Mital, S. & Mercimek-Mahmutoglu, S. Progressive Cerebellar Atrophy and a Novel Homozygous Pathogenic DNAJC19 Variant as a Cause of Dilated Cardiomyopathy Ataxia Syndrome. *Pediatr. Neurol.* **62**, 58–61 (2016).

10.   Sparkes, R., Patton, D. & Bernier, F. Cardiac features of a novel autosomal recessive dilated cardiomyopathic syndrome due to defective importation of mitochondrial protein. *Cardiol. Young* **17**, 215–217 (2007).

11.   Rohani, L. *et al.* Modeling the Dilated Cardiomyopathy with Ataxia Syndrome (DCMA) , A Pediatric Mitochondrial Cardoimyopathy, Using Cardiomyocytes Derived from Induced Pluripotent Stem Cells. *Can. J. Cardiol.* **33**, S163–S164 (2017).

12.   Das, J. The role of mitochondrial respiration in physiological and evolutionary adaptation. *BioEssays* **28**, 890–901 (2006).

13.   Brown, D. A. *et al.* Expert consensus document: Mitochondrial function as a therapeutic target in heart failure. *Nat. Rev. Cardiol.* **14**, 238–250 (2017).

14.   Squire, J. M. Architecture and function in the muscle sarcomere. *Curr. Opin. Struct. Biol.* **7**, 247–257 (1997).

15.   Sequeira, V. & van der Velden, J. Historical perspective on heart function: the Frank-Starling Law. *Biophys. Rev.* **7**, 421–447 (2015).

16.   Berk, F. *et al.* Assessment of left ventricular function and volumes for patients with

dilated cardiomyopathy using gated myocardial perfusion spect and comparison with echocardiography. *Nucl. Med. Commun.* **26**, 701–710 (2005).

17. Xie, B. Q. *et al.* Evaluation of left and right ventricular ejection fraction and volumes from gated blood-pool SPECT in patients with dilated cardiomyopathy: Comparison with cardiac MRI. *J. Nucl. Med.* **53**, 584–591 (2012).

18. Roesch, K. Human deafness dystonia syndrome is caused by a defect in assembly of the DDP1/TIMM8a-TIMM13 complex. *Hum. Mol. Genet.* **11**, 477–486 (2002).

19. Stetler, R. A. *et al.* Heat Shock Proteins: Cellular and molecular mechanisms in the CNS. *Prog. Neurobiol.* **92**, 184–211 (2010).

20. Boengler, K., Heusch, G. & Schulz, R. Nuclear-encoded mitochondrial proteins and their role in cardioprotection. *Biochim. Biophys. Acta* **1813**, 1286–1294 (2011).

21. Richter-Dennerlein, R. *et al.* DNAJC19, a Mitochondrial Cochaperone Associated with Cardiomyopathy, Forms a Complex with Prohibitins to Regulate Cardiolipin Remodeling. *Cell Metab.* **20**, 158–171 (2014).

22. Ye, C., Shen, Z. & Greenberg, M. L. Cardiolipin remodeling: a regulatory hub for modulating cardiolipin metabolism and function. *Journal of Bioenergetics and Biomembranes* **48**, 113–123 (2016).

23. Chowdhury, A. *et al.* Defective Mitochondrial Cardiolipin Remodeling Dampens HIF-1α Expression in Hypoxia. *Cell Rep.* **25**, 561-570.e6 (2018).

24. Paradies, G., Paradies, V., De Benedictis, V., Ruggiero, F. M. & Petrosillo, G. Functional role of cardiolipin in mitochondrial bioenergetics. *Biochim. Biophys. Acta - Bioenerg.* **1837**, 408–417 (2014).

25. Siasos, G. *et al.* Mitochondria and cardiovascular diseases—from pathophysiology to treatment. *Ann. Transl. Med.* **6**, 256–256 (2018).

26. Finsterer, J. Barth syndrome: Mechanisms and management. *Appl. Clin. Genet.* **12**, 95–106 (2019).

27. Saric, A., Andreau, K., Armand, A. S., Møller, I. M. & Petit, P. X. Barth syndrome: From mitochondrial dysfunctions associated with aberrant production of reactive oxygen species to pluripotent stem cell studies. *Frontiers in Genetics* **6**, (2016).

28. Rohani, L. *et al.* Reversible Mitochondrial Fragmentation in iPSC-Derived Cardiomyocytes from Children with DCMA, a Mitochondrial Cardiomyopathy. *Can. J. Cardiol.* 732339 (2019). doi:10.1016/j.cjca.2019.09.021

29. Machiraju, P. *et al.* SS-31 Reverses Mitochondrial Fragmentation in Fibroblasts from Patients with DCMA, a Mitochondrial Cardiomyopathy. *bioRxiv* 672857 (2019). doi:10.1101/672857

30. Huttlin, E. L. *et al.* Architecture of the human interactome defines protein communities and disease networks. *Nature* **545**, 505–509 (2017).

31. Schweppe, D. K., Huttlin, E. L., Harper, J. W. & Gygi, S. P. BioPlex Display: An Interactive Suite for Large-Scale AP–MS Protein–Protein Interaction Data. *J. Proteome Res.* **17**, 722–726 (2018).

32. Wortmann, S. B., Kluijtmans, L. A., Engelke, U. F. H., Wevers, R. A. & Morava, E. The 3-methylglutaconic acidurias: what's new? *J. Inherit. Metab. Dis.* **35**, 13–22 (2012).

33. Jellum, E., Kvittingen, E. A. & Stokke, O. Mass spectrometry in diagnosis of metabolic disorders. *Biomed. Environ. Mass Spectrom.* **16**, 57–62 (1988).
34. Hoitzing, H., Johnston, I. G. & Jones, N. S. What is the function of mitochondrial networks? A theoretical assessment of hypotheses and proposal for future research. *BioEssays* **37**, 687–700 (2015).
35. Scott, I. & Youle, R. J. Mitochondrial fission and fusion. *Essays Biochem.* **47**, 85–98 (2010).
36. Osellame, L. D., Blacker, T. S. & Duchen, M. R. Cellular and molecular mechanisms of mitochondrial function. *Best Practice and Research: Clinical Endocrinology and Metabolism* **26**, 711–723 (2012).
37. Gross, M. I. *et al.* Antitumor activity of the glutaminase inhibitor CB-839 in triple-negative breast cancer. *Mol. Cancer Ther.* **13**, 890–901 (2014).
38. Rogatzki, M. J., Ferguson, B. S., Goodwin, M. L. & Gladden, L. B. Lactate is always the end product of glycolysis. *Front. Neurosci.* **9**, (2015).
39. Chen, Q. *et al.* Rewiring of Glutamine Metabolism Is a Bioenergetic Adaptation of Human Cells with Mitochondrial DNA Mutations. *Cell Metab.* **27**, 1007–1025 (2018).
40. Fernie, A. R., Carrari, F. & Sweetlove, L. J. Respiratory metabolism: Glycolysis, the TCA cycle and mitochondrial electron transport. *Current Opinion in Plant Biology* **7**, 254–261 (2004).
41. Blacker, T. S. & Duchen, M. R. Investigating mitochondrial redox state using NADH and NADPH autofluorescence. *Free Radical Biology and Medicine* **100**, 53–65 (2016).
42. Mitchell, P. Coupling of phosphorylation to electron and hydrogen transfer by a chemi-osmotic type of mechanism. *Nature* **191**, 144–148 (1961).
43. Maloney, P. C., Kashket, E. R. & Wilson, T. H. A protonmotive force drives ATP synthesis in bacteria. *Proc. Natl. Acad. Sci. U. S. A.* **71**, 3896–3900 (1974).
44. Meléndez-Rodríguez, F. *et al.* HIF1α Suppresses Tumor Cell Proliferation through Inhibition of Aspartate Biosynthesis. *Cell Rep.* **26**, 2257-2265.e4 (2019).
45. Conway, M. E. Aminotransferases. in *Amino Acids in Human Nutrition and Health* 24–50 (CABI Publishing, 2011). doi:10.1079/9781845937980.0024
46. Plaitakis, A., Kalef-Ezra, E., Kotzamani, D., Zaganas, I. & Spanaki, C. The glutamate dehydrogenase pathway and its roles in cell and tissue biology in health and disease. *Biology* **6**, (2017).
47. Bhutia, Y. D. & Ganapathy, V. Glutamine transporters in mammalian cells and their functions in physiology and cancer. *Biochimica et Biophysica Acta - Molecular Cell Research* **1863**, 2531–2539 (2016).
48. Jang, C., Chen, L. & Rabinowitz, J. D. Metabolomics and Isotope Tracing. *Cell* **173**, 822–837 (2018).
49. Koletzko, B. *et al.* The use of stable isotope techniques for nutritional and metabolic research in paediatrics. in *Early Human Development* **53**, (1998).
50. Yuan, J., Bennett, B. D. & Rabinowitz, J. D. Kinetic flux profiling for quantitation of cellular metabolic fluxes. *Nat. Protoc.* **3**, 1328–1340 (2008).
51. Zhang, J. *et al.* 13C isotope-assisted methods for quantifying glutamine metabolism in cancer cells. *Methods Enzymol.* **542**, 369–89 (2014).

52.   Foschi, F. G. *et al.* Urea cycle disorders: A case report of a successful treatment with liver transplant and a literature review. *World J. Gastroenterol.* **21**, 4063–4068 (2015).

53.   Ikon, N. & Ryan, R. O. Cardiolipin and mitochondrial cristae organization. *Biochim. Biophys. Acta - Biomembr.* **1859**, 1156–1163 (2017).

54.   Tiefenthaler, M. *et al.* Increased lactate production follows loss of mitochondrial membrane potential during apoptosis of human leukaemia cells. *Br. J. Haematol.* **114**, 574–580 (2001).

55.   Chinopoulos, C. & Seyfried, T. N. Mitochondrial Substrate-Level Phosphorylation as Energy Source for Glioblastoma: Review and Hypothesis. *ASN Neuro* **10**, (2018).

56.   van der Windt, G. J. W., Chang, C. H. & Pearce, E. L. Measuring bioenergetics in T cells using a seahorse extracellular flux analyzer. *Curr. Protoc. Immunol.* **2016**, 3.16B.1-3.16B.14 (2016).

57.   Mookerjee, S. A., Goncalves, R. L. S., Gerencser, A. A., Nicholls, D. G. & Brand, M. D. The contributions of respiration and glycolysis to extracellular acid production. *Biochim. Biophys. Acta - Bioenerg.* **1847**, 171–181 (2015).

58.   Zhang, J. *et al.* Measuring energy metabolism in cultured cells, including human pluripotent stem cells and differentiated cells. *Nat. Protoc.* **7**, 1068–1085 (2012).

59.   Urban, P. L. Quantitative mass spectrometry: An overview. *Philosophical Transactions of the Royal Society A: Mathematical, Physical and Engineering Sciences* **374**, (2016).

60.   Scalise, M., Pochini, L., Galluccio, M., Console, L. & Indiveri, C. Glutamine transport and mitochondrial metabolism in cancer cell growth. *Frontiers in Oncology* **7**, (2017).

61.   Kostidis, S., Addie, R. D., Morreau, H., Mayboroda, O. A. & Giera, M. Quantitative NMR analysis of intra- and extracellular metabolism of mammalian cells: A tutorial. *Anal. Chim. Acta* **980**, 1–24 (2017).

62.   Boraldi, F., Annovi, G., Tiozzo, R., Sommer, P. & Quaglino, D. Comparison of ex vivo and in vitro human fibroblast ageing models. *Mech. Ageing Dev.* **131**, 625–635 (2010).

63.   Janson, D., Rietveld, M., Willemze, R. & El Ghalbzouri, A. Effects of serially passaged fibroblasts on dermal and epidermal morphogenesis in human skin equivalents. *Biogerontology* **14**, 131–140 (2013).

64.   Lemons, J. M. S. *et al.* Quiescent fibroblasts exhibit high metabolic activity. *PLoS Biol.* **8**, (2010).

65.   Lu, W. *et al.* Metabolomic analysis via reversed-phase ion-pairing liquid chromatography coupled to a stand alone orbitrap mass spectrometer. *Anal. Chem.* **82**, 3212–21 (2010).

66.   Silvestro, L., Tarcomnicu, I. & Savu, S. R. Matrix Effects in Mass Spectrometry Combined with Separation Methods — Comparison HPLC, GC and Discussion on Methods to Control these Effects. in *Tandem Mass Spectrometry - Molecular Characterization* (InTech, 2013). doi:10.5772/55982

67.   Buescher, J. M. *et al.* A roadmap for interpreting 13C metabolite labeling patterns from cells. *Current Opinion in Biotechnology* **34**, 189–201 (2015).

68. Lu, W. *et al.* Metabolite Measurement: Pitfalls to Avoid and Practices to Follow. *Annu. Rev. Biochem.* **86**, 277–304 (2017).

69. Melamud, E., Vastag, L. & Rabinowitz, J. D. Metabolomic analysis and visualization engine for LC - MS data. *Anal. Chem.* **82**, 9818–9826 (2010).

70. Doenst, T., Nguyen, T. D. & Abel, E. D. Cardiac metabolism in heart failure: Implications beyond atp production. *Circ. Res.* **113**, 709–724 (2013).

71. Tanner, L. B. *et al.* Four Key Steps Control Glycolytic Flux in Mammalian Cells. *Cell Syst.* **7**, 49-62.e8 (2018).

72. Vangipuram, M., Ting, D., Kim, S., Diaz, R. & Schüle, B. Skin punch biopsy explant culture for derivation of primary human fibroblasts. *J. Vis. Exp.* (2013). doi:10.3791/3779

73. Mullen, A. R. *et al.* Reductive carboxylation supports growth in tumour cells with defective mitochondria. *Nature* **481**, 385–388 (2012).

74. Mescam, M., Vinnakota, K. C. & Beard, D. A. Identification of the catalytic mechanism and estimation of kinetic parameters for fumarase. *J. Biol. Chem.* **286**, 21100–21109 (2011).

75. Hamanaka, R. B. *et al.* Glutamine Metabolism Is Required for Collagen Protein Synthesis in Lung Fibroblasts. *Am. J. Respir. Cell Mol. Biol.* **61**, 597–606 (2019).

76. Ballester, M. *et al.* Glutamine/glutamate metabolism rewiring in reprogrammed human hepatocyte-like cells. *Sci. Rep.* **9**, (2019).

77. Nissim, I., Brosnan, M. E., Yudkoff, M., Nissim, I. & Brosnan, J. T. Studies of hepatic glutamine metabolism in the perfused rat liver with 15N-labeled glutamine. *J. Biol. Chem.* **274**, 28958–28965 (1999).

78. Soria, L. R. *et al.* Aquaporin-8-facilitated mitochondrial ammonia transport. *Biochem. Biophys. Res. Commun.* **393**, 217–221 (2010).

79. Yang, N. J. & Hinner, M. J. Getting across the cell membrane: an overview for small molecules, peptides, and proteins. *Methods in molecular biology (Clifton, N.J.)* **1266**, 29–53 (2015).

80. Lane, A. N. & Fan, T. W. M. Regulation of mammalian nucleotide metabolism and biosynthesis. *Nucleic Acids Research* **43**, 2466–2485 (2015).

81. Olalla, L. *et al.* Nuclear localization of L-type glutaminase in mammalian brain. *J. Biol. Chem.* **277**, 38939–38944 (2002).

82. Perera, S. Y., Voith, D. M. & Curthoyst, N. P. *Biosynthesis and processing of mitochondrial glutaminase in HTC hepatoma cells. Biochem. J* **273**, (1991).

83. Zerangue, N. & Kavanaugh, M. P. *Flux coupling in a neuronal glutamate transporter*.

84. Goubert, E. *et al.* Inhibition of the mitochondrial glutamate carrier SLC25A22 in astrocytes leads to intracellular glutamate accumulation. *Front. Cell. Neurosci.* **11**, (2017).

85. Fiermonte, G. *et al.* Identification of the mitochondrial glutamate transporter. Bacterial expression, reconstitution, functional characterization, and tissue distribution of two human isoforms. *J. Biol. Chem.* **277**, 19289–19294 (2002).

86. Bailey, C. G. *et al.* Loss-of-function mutations in the glutamate transporter SLC1A1 cause human dicarboxylic aminoaciduria. *J. Clin. Invest.* **121**, 446–453 (2011).

87. Greenway, S. C., Dallaire, F., Hazari, H., Patel, D. & Khan, A. Addition of Digoxin Improves Cardiac Function in Children With the Dilated Cardiomyopathy With Ataxia Syndrome: A Mitochondrial Cardiomyopathy. *Can. J. Cardiol.* **34**, 972–977 (2018).

88. Finkel, T. *et al.* The ins and outs of mitochondrial calcium. *Circulation Research* **116**, 1810–1819 (2015).

89. Sakurai, T. *et al.* Slc25a12 Disruption Alters Myelination and Neurofilaments: A Model for a Hypomyelination Syndrome and Childhood Neurodevelopmental Disorders. *Biol. Psychiatry* **67**, 887–894 (2010).

90. Szeto, H. H. First-in-class cardiolipin-protective compound as a therapeutic agent to restore mitochondrial bioenergetics. *British Journal of Pharmacology* **171**, 2029–2050 (2014).

91. Escribano-Lopez, I. *et al.* The mitochondrial antioxidant SS-31 increases SIRT1 levels and ameliorates inflammation, oxidative stress and leukocyte-endothelium interactions in type 2 diabetes. *Sci. Rep.* **8**, (2018).

92. Wu, J. *et al.* Elamipretide (SS-31) ameliorates isoflurane-induced long-term impairments of mitochondrial morphogenesis and cognition in developing rats. *Front. Cell. Neurosci.* **11**, (2017).

93. Ma, X. *et al.* Mitochondrial electron transport chain complex III is required for antimycin A to inhibit autophagy. *Chem. Biol.* **18**, 1474–1481 (2011).

94. Schindelin, J. *et al.* Fiji: An open-source platform for biological-image analysis. *Nature Methods* **9**, 676–682 (2012).

95. Ježek, J., Cooper, K. F. & Strich, R. Reactive oxygen species and mitochondrial dynamics: The yin and yang of mitochondrial dysfunction and cancer progression. *Antioxidants* **7**, (2018).